Chapter 1 Introduction

The pyramid-like structures on Ⅲ-Ⅴ compound semiconductors surfaces have been widely discussed. These structures are formed spontaneously[1-6] or artificially[7-12], and they all have particular optical and electrical properties. For example, some researches have studied the emission characteristics on artificial pyramid-like structures[7-11] with the aid of high spatial resolution, and results showed that the emissions from apex and sidewall are quite different. Besides the artificial pyramid-like structures, other studies focused on the spontaneously-formed pyramid-like structures, including the formation mechanism[13-16], the optical properties[17-19], and the electrical properties[20].

The purpose of this thesis is to study the stress influence on hillocks and how deep hillocks are formed. We examined spontaneously formed hexagonal hillocks on $Al_xGa_{1-x}N$ thin film. By using a microscope to demarcate the hillock position, we can study the same hillock on this sample and analyze the stress influence on various sizes of hillock, combining the μ-PL and μ-Raman measurements.

There are five chapters in this thesis, including this chapter " Introduction ". In chapter 2 , we briefly describe the structure, optical transition, and Raman scattering of Ⅲ-Nitride semiconductors. In

Chapter 3, we give details of the sample preparation and the experimental setup. In chapter 4, we combine the μ-PL and μ-Raman results to analyze the stress influence on tent-like hillock. In addition, the μ-Raman depth analysis has shown how deep hillocks are formed. Finally, in chapter 5, we summarize the experimental results of AlGaN hillocks.

Chapter 2 Theoretical Background

2-1 Wurtzite Structure and Related Raman Tensors

The wurzite structure is very similar to the more basic zinc-blende (ZB) structure as shown in Fig. 2-1-1. In fact, they are actually identical to the nearest-neighbor shell. Therefore, the dispersion curves or the wurzite may be deduced from those of the zinc-blende by folding the brillouin zone (BZ) along the $\Lambda(111)$ direction. The main difference between these two structures is in the stacking sequence of the closest packed diatomic planes, the stacking sequence is ABABAB$\cdots$ in the <0001> direction for the wurtzite structure, and ABCABC$\cdots$ in the <111> direction for the ZB structure.

Gallium nitride crystallizes in the hexagonal wurzite structure in a unit cell and belongs to C_6^v point group[21]. The group theory predicts two A_1, two E_1, two E_2 and two B_1 irreducible representations at the Γ point in BZ as the following,

$$\Gamma = 2A_1 + 2B_1 + 2E_1 + 2E_2 \qquad (2\text{-}1\text{-}1)$$

However, one A_1 and E_1 are acoustic vibrations while the B_1 mode is silent[22]. The E_2 modes are Raman-active, the A_1 and the E_1 modes are both Raman and infrared active. Due to the long-range Coulomb field, the

polar A_1 and E_1 modes split the LO and TO modes. So there are six Raman-active phonons.

The Raman tensors for the C_{6v} point group are expressed by the susceptibility matrix $\overset{\leftrightarrow}{\chi}$ in the following forms:

$$A_1 \text{ mode } \begin{bmatrix} a & 0 & 0 \\ 0 & a & 0 \\ 0 & 0 & b \end{bmatrix}$$

$$E_1 \text{ mode } \begin{bmatrix} 0 & 0 & c \\ 0 & 0 & 0 \\ c & 0 & 0 \end{bmatrix} \text{ and } \begin{bmatrix} 0 & 0 & 0 \\ 0 & 0 & c \\ 0 & c & 0 \end{bmatrix}$$

$$E_2 \text{ mode } \begin{bmatrix} d & 0 & 0 \\ 0 & -d & 0 \\ 0 & 0 & 0 \end{bmatrix} \text{ and } \begin{bmatrix} 0 & -d & 0 \\ -d & 0 & 0 \\ 0 & 0 & 0 \end{bmatrix}$$

The scattering matrix element is formed by taking the product of the susceptibility matrix $\overset{\leftrightarrow}{\chi}$ with the incident $\vec{\varepsilon}_i$ and scattered $\vec{\varepsilon}_s$ polarization vectors in the form of $\left| \vec{\varepsilon}_i \cdot \overset{\leftrightarrow}{\chi} \cdot \vec{\varepsilon}_s \right|$ [23]. It is non-zero for Raman active modes for particular combinations of $\vec{\varepsilon}_i$ and $\vec{\varepsilon}_s$. Table 2-1-1 shows the Raman selection rules of the hexagonal Ⅲ-N.
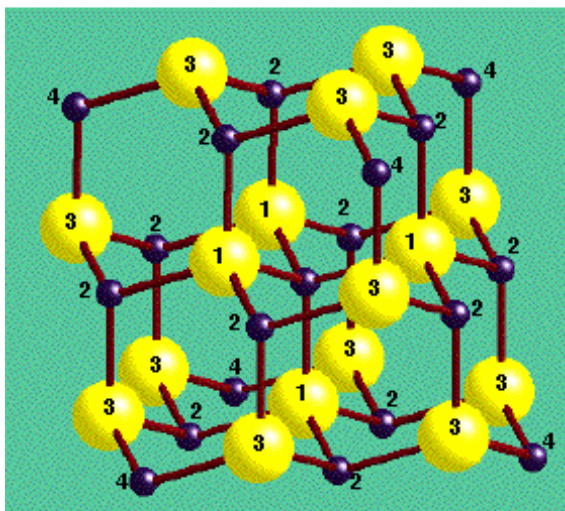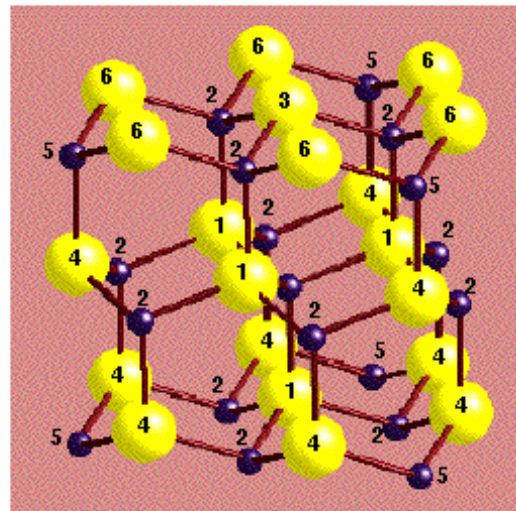
PLANE VIEWS
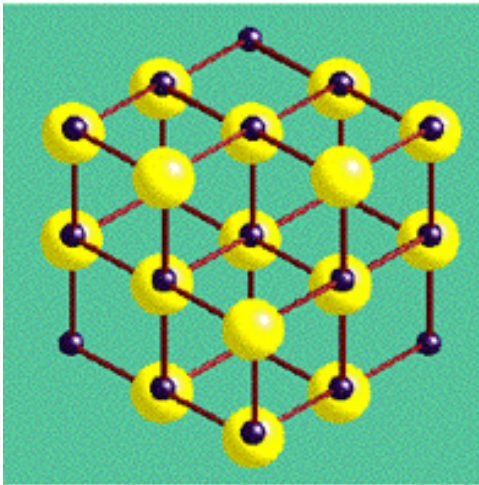
Zinc Blende
CCP ABC repeat
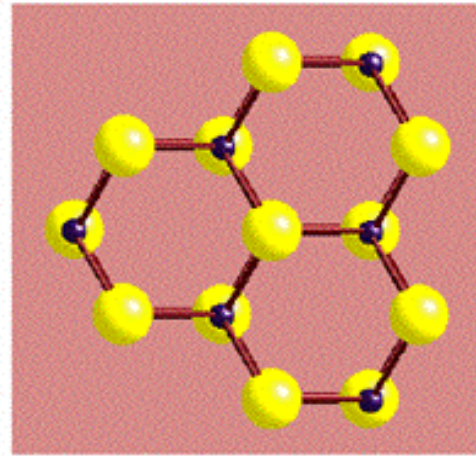
Wurtzite
HCP AB repeat

Fig. 2-1-1 (a)

COORDINATION ENVIRONMENTS

Zinc Blende

Wurtzite

Fig. 2-2-1 (b)

http://www.chem.ox.ac.uk/.../ Lecture2/Lec2.html

Scattering configuration	Allowed modes
$z(yy)\bar{z}$	$E_2(TO)$ ， $A_1(LO)$
$z(yx)\bar{z}$	$E_2(TO)$
$y(xx)\bar{y}$	$A_1(TO)$
$y(xz)\bar{y}$	$E_1(TO)$
$z(\overline{yy})\bar{z}$	$E_2(TO)$ ， $A_1(TO)$
$z(\overline{yx})\bar{z}$	$E_1(TO)$ ， $E_1(LO)$

Raman selection rules for optical phonons in wurtzite crystal.

Table 2-1-1 The selection rule for hexagonal structures.

2-2　Photoluminescence in Semiconductors

　　Photoluminescence (PL) is one of the useful optical methods for the semiconductor. Its ability is powerful and sensitive to find impurities and defects in silicon and group III-V element semiconductors, which affect materials quality and device performance. This fingerprint identifies the impurity type, and often several different impurities can be seen in a single PL spectrum. Luminescence may involve radiative electronic transitions emitting a photon when an electron drops from an upper to a lower energy level of either intrinsic band state or impurity level. Two types of recombination are described as follows[24][25][26]:

(A) Radiative Transition

(I) Band to Band Transition

　　Band to band transitions involving free electrons and holes usually occur in direct gap materials, such as III-V compounds, between conduction and valence bands with conservation of momentum. The e-h pairs will recombine radiatively with a high probability. The total e-h recombination rate is given by

$$R = \int R(h\nu)d(h\nu) \approx np \qquad\qquad (2\text{-}2\text{-}1)$$

where n, p is the electron and hole concentration respectively, h is Planck's constant, ν is the frequency of emitted photon. It shows the higher free carrier, the higher recombination rate.

(II) Free Exciton Transition

Free excitons (FE) represent the lowest energy intrinsic excitation of electrons and holes in pure materials at low excitation density. The energy of free excitons is given by

$$E_n = \frac{2\pi^2 m^* e^4}{h^2 \varepsilon^2 n^2} \qquad (2\text{-}2\text{-}2)$$

where m^* is the reduced mass, n the quantum number, ε the dielectric constant. The FE results in a lowering of the total energy of the e-h pair as $hv = E_g - E_n$.

(III) Donor Acceptor Pair Recombination (DAP)

By optical excitation, electrons and holes can be created at the D^+ and A^- sites to produce neutral D^0 and A^0 centers. In returning to equilibrium, some of the electrons on the neutral donors will recombine radiatively with holes on the neutral acceptors. Transition between donors (activators) and acceptors (co-activators) levels can be represented by the reaction,

$$D^0 + A^0 \rightarrow hv + D^+ + A^- \qquad (2\text{-}2\text{-}3)$$

The energy E_{DAP} of a photon emitted from such a transition would be

$$E_{DAP} = hv = E_g - (E_D - E_A) + \frac{Q^2}{\varepsilon R_{DAP}} \qquad (2\text{-}2\text{-}4)$$

where E_D and E_A is the binding energy of donor and acceptor, respectively, Q the charge, ε the dielectric constant of the material, and R_{DAP} is the distance between the donor and the acceptor.

(B) Non-Radiative Transition

There are several transitions that compete with the radiative transition that reduce the emission efficiency. They are described as follows :

(I)   The e-h pair is scattered by the phonon or carriers and loses its energy.

(II)   The e-h pair recombines at defect, dislocation, grain boundary or surface, and loses its excess energy, the so-called "cascade process".

(III) The e-h pair loses its energy via the " Auger process " that involves the core level transitions.

The more the non-radiation transition, the lower the PL intensity.
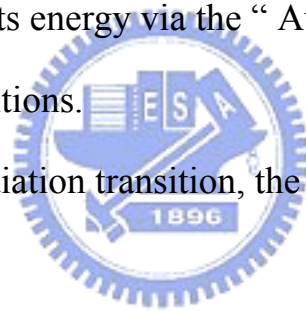
2-3　Raman Scattering

The inelastic scattering phenomenon was first discovered in 1928 by Sir Chandrasekhera Venkata Raman. Raman spectroscopy is an excellent probe to investigate the low energy elementary excitations in materials as well as to characterize their structural, electronic, vibrational and magnetic properties. When light is scattered from a molecule, most photons are elastically scattered. The scattered photons have the same energy (frequency) and, therefore, wavelength, as the incident photons. However, a small fraction of light (approximately 1 in 10^7 photons) is scattered at optical frequencies different from, and usually lower than, the frequency of the incident photons. The process leading to this inelastic scattering is named the Raman effect. Raman scattering can occur with a change in vibrational, rotational or electronic energy of a molecule.

Fig. 2-3-1 shows Stokes scattering and anti-Stokes scattering. The photon frequency is shifted after interacting with a phonon. If the phonon creates in the interaction, the photon energy would be shifted toward lower frequency, the so called "Stokes scattering". On the other hand, if the phonon is absorbed in the interaction, the photon energy would be shifted toward higher frequency, it is the "Anti-Stokes scattering". All these processes must obey the energy and the momentum conservation laws.

$$\hbar\omega_R = \hbar\omega_i \pm \hbar\Omega_{phonon}$$

$$\vec{k}_R = \vec{k}_i \pm \vec{k}_{phonon}$$

where $\hbar\omega_R$ and $\vec{k}_R$ are the scattered photon energy and momentum, $\hbar\omega_i$ and $\vec{k}_i$ are the incident photon energy and momentum, $\hbar\Omega_{phonon}$ and $\vec{k}_{phonon}$ are the phonon energy and momentum, respectively. The phonon frequency can be expressed as[27] :

$$\Omega(\vec{k})_{phonon} = \sqrt{\frac{\lambda(\vec{k})}{M}}$$

where $\lambda(\vec{k})$ is the force constant with wave vector $\vec{k}$ and $\vec{k}$ is a function of lattice constant. If the strain or the composition changes, the lattice constant will also change and affect the phonon frequency. According to the shift of the phonon frequency, we may analyze the crystalline structure.

Virtual State

Vibrational Levels
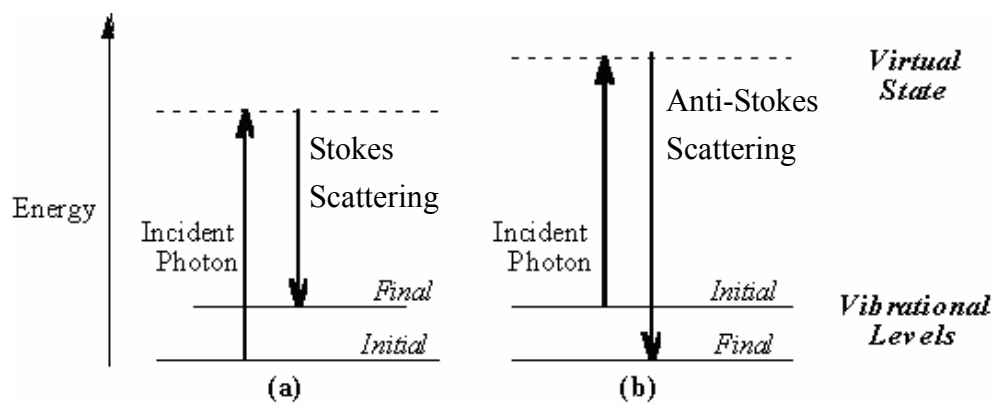
Fig. 2-3-1

Energy level diagram for Raman scattering; (a) Stokes

Raman scattering (b) anti-Stokes Raman scattering.

Chapter 3 Experiments

3-1　Sample Preparation

The $Al_xGa_{1-x}N$ thin film sample, obtained from the "Chung-Shan Institute of Science and Technology ", was grown by the Low Pressure Metalorganic Chemical Vapor Deposition (MOCVD) system (AIXTRON 200). The system is equipped with a horizontal quartz reactor, with the radio- frequency (RF) as the heating source. The $Al_xGa_{1-x}N$ thin film was deposited on the (0001) sapphire, by using Trimethylgallium (TMGa) 、 Trimethylaluminum (TMAl)、Ammonia (NH_3) as the Ga、Al、N sources, and the high- purity H_2 as the carrier gas. Prior to growth, the substrate was sent to the reactor and thermally cleaned under the hydrogen ambient at 1120 ℃ for 10 minutes. In order to minimize the lattice mismatch between the thin film and sapphire, we deposited an aluminum nitride (AlN) buffer layer about 25nm first. Then aluminum gallium nitride ($Al_xGa_{1-x}N$) thin film about 0.7 μm was grown on the top of buffer layer.

3-2　Micro-PL system

The Micro-PL system incorporated an Olympus BH2 optical microscope. The system is shown in Fig. 3-2-1. The He-Cd laser operated at 325nm (Omnichrome 2074-M-A02) is the light source. The beam was reflected by an UV mirror and then incident into the microscope, passing through a beam splitter and focused by the near-UV objective lens (Mitutoyo NUV 100X , N.A.=0.5). The focused spot is detected by a color CCD camera (Sony Exwave HAD), with a diameter $\leqq 3$ μm. The luminescence signals from the laser beam were collected by the objective lens, then reflected by the beam splitter, through the long pass filter to cut off the laser signals. Finally, the PL signals were sent into the optical fiber, and dispersed by the monochrometor (ARC Pro 500) and detected by the photomultiplier tube (PMT Hamamatsu R955). As the entrance and exit slits of the monochromator were both set to 50 μm, the spectral resolution was about 0.2 nm. All signals were processed by the LabView-based software.

Micro-Photoluminescence system
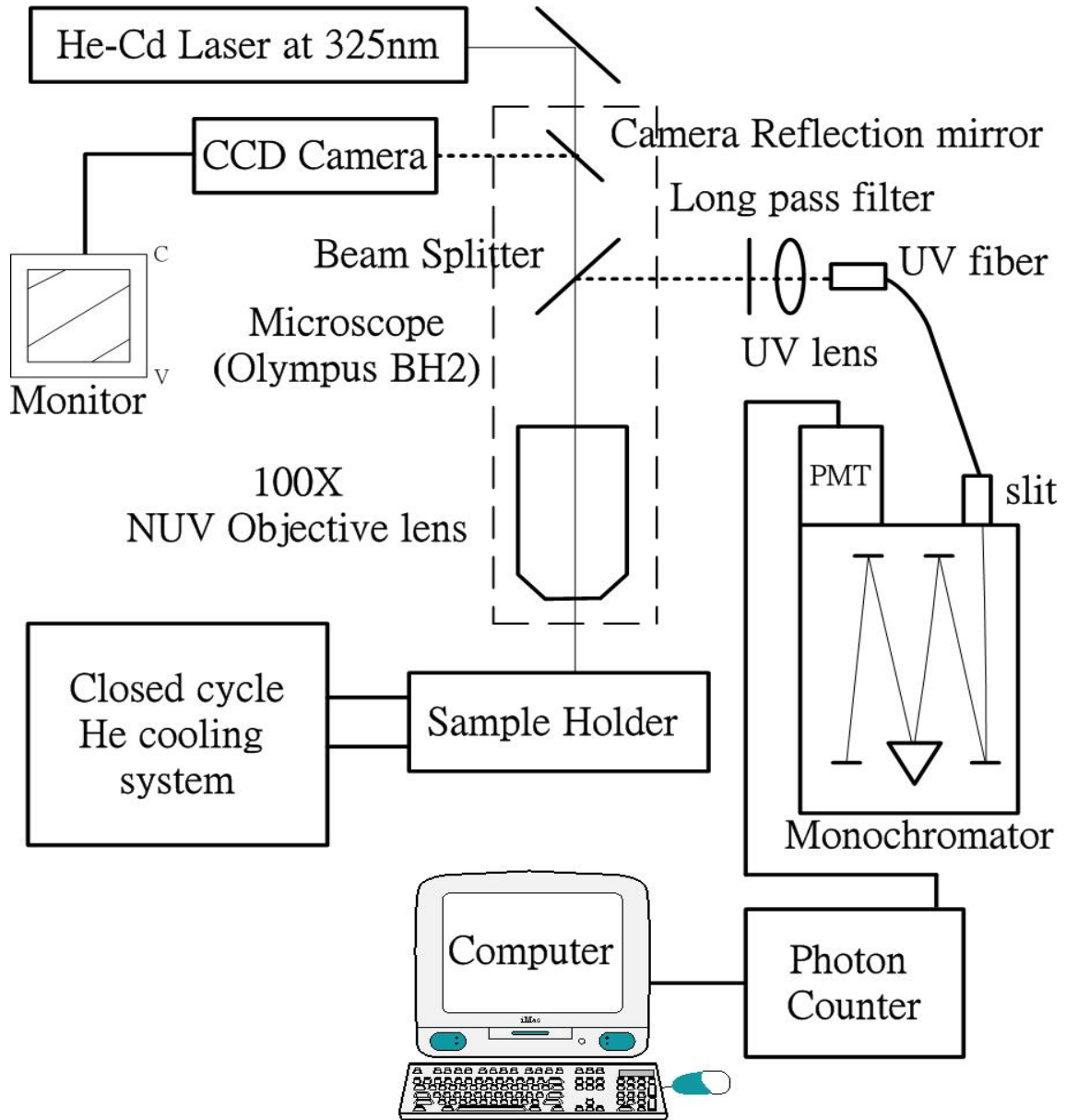
Fig. 3-2-1

3-3　Micro-Raman system

The Micro-Raman system was manufactured by Jobin-Yvon corporation. The system is shown in Fig. 3-3-1. It consists of an Olympus BX-40 confocal microscope, a Raman spectrometer, and a water cooled CCD detector. The laser beam (at 488nm) is from the Coherent Innova 70C-A6 multiline visible laser, reflected by five UV mirrors, and then incident into the system. To cut off the laser plasma line, an inteference filter (at 488 nm) was inserted. After reflecion by a mirror and a notch filter (at 488 nm), the beam was guided into the microscope, and focused by the objective lens (Olympus 100X N.A.= 0.9), with the spot size on the sample about 2 μm. The Raman signals from the sample and the laser signals reflected by the sample were both collected by the objective lens. However, after the notch filter, only the Raman signals passed and were guided into the Raman spectrometer. This Raman spectrometer is equipped with a double grating (1800 g/mm), with the spectral resolution is ~0.5 cm^{-1} while the slit opening is 100μm. Finally, the dispersed Raman signals will be collected by the CCD detector .　.

Micro-Raman system
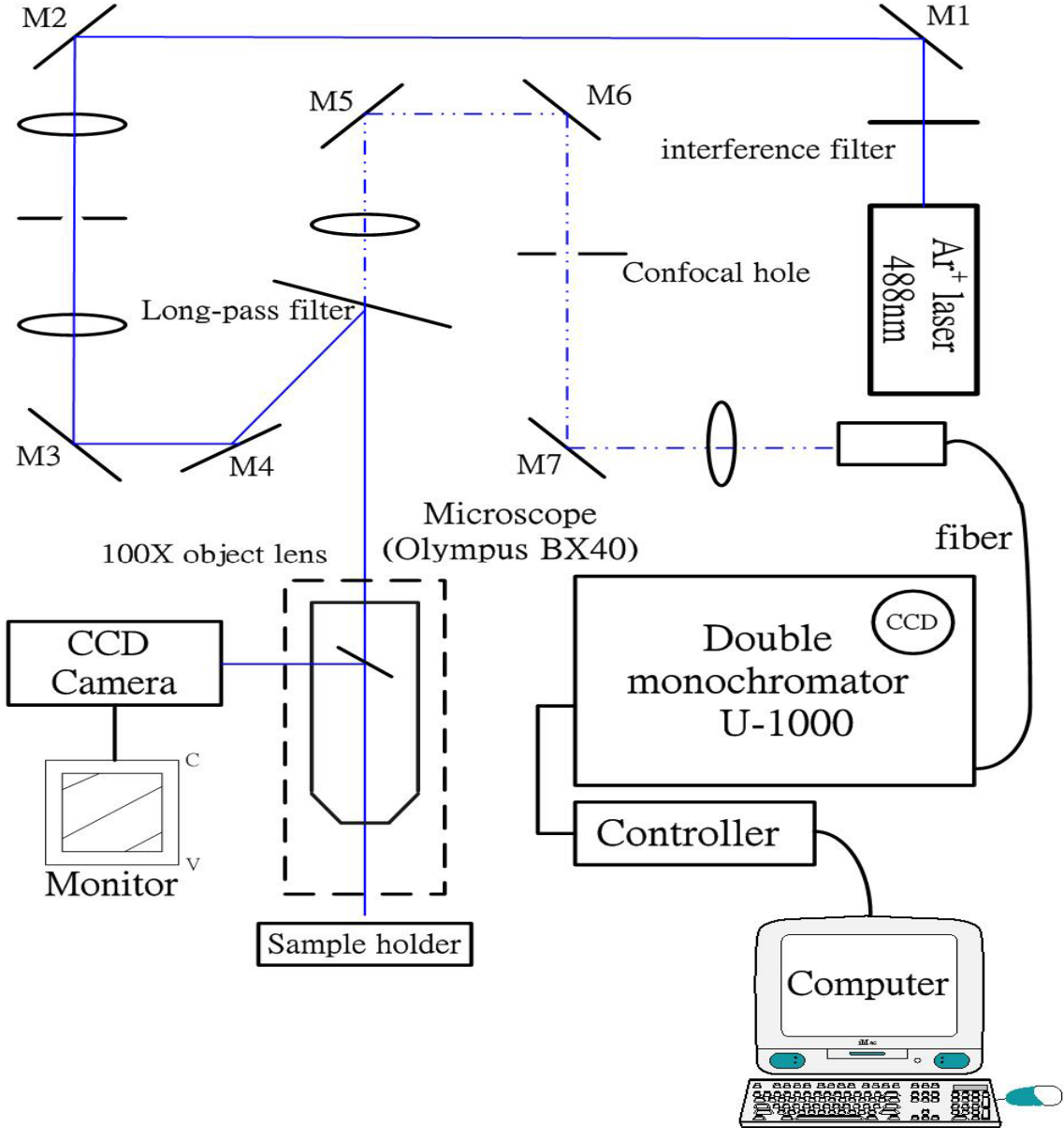
Fig. 3-3-1

Chapter 4 Results and Discussion

In this chapter, we present experimental results of the hexagonal hillocks on $Al_xGa_{1-x}N$ film. We used spatially resolved μ-PL and μ-Raman techniques to study the photo-carriers recombination mechanism and the phonon distribution. By correlating the μ-PL and μ-Raman results, the influence of stress on hillocks is elucidated.

4-1　The Types of Hillocks

As shown in SEM pictures of Fig. 4-1-1, there are three types of hillocks on AlGaN sample. The first one called pyramid-like hillock, is distributed extensively on the sample and the angle between the sidewall and the plane region is about 3°; the second one called mesa-like hillock, has a quasi-flat top and the angle between the sidewall and the plane region is about 55°; the third one called tent-like hillock, has two-step sidewall, and the angle between plane region and bottom sidewall is about 22° while the upper sidewall is about 13°. The size distribution is about 3~5μm and 6 ~11μm for mesa and tent-like hillocks, respectively. In this paper, we will look into the stress influence on the optical and phonon properties of different hillock type and size.

~ 300~600nm

~3°
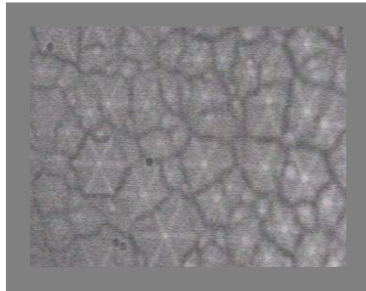
~5-8μm
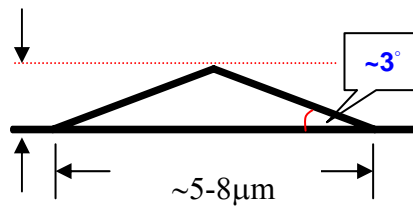
pyramid-like

~ 400~700nm

5°

55°

~ 3-5μm

mesa-like

~1000 nm

13°

20°
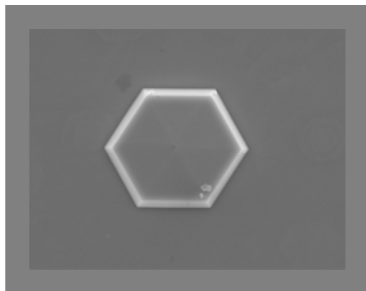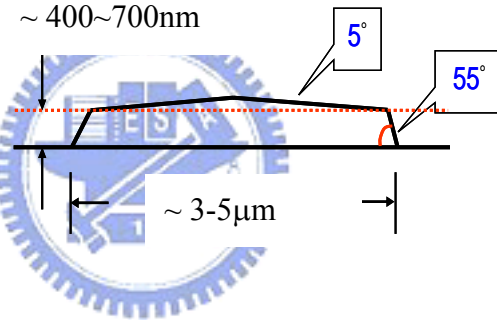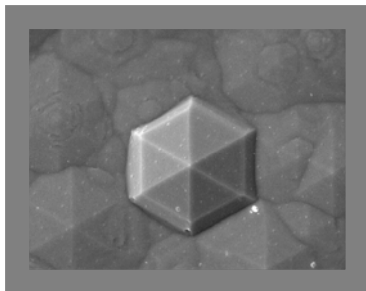
> 6μm
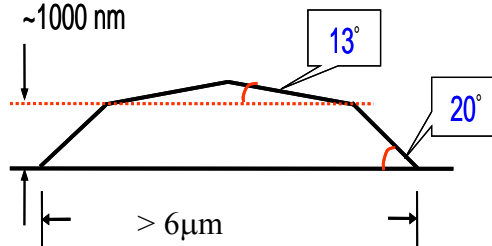
tent-like

Fig. 4-1-1

4-2 The Correlation of Micro-PL and Micro-Raman at the Same Hillocks

In our previous studies [28] [29], interesting optical properties inside hillocks have been revealed. The μ-PL results showed that an additional peak I_H appears inside the hillock besides the near-band-edge emission (NBE) at ~ 342nm as shown in Fig.4-2-1. This extra peak is much stronger than the NBE.

Since the photoluminescence peak shift may be caused by compositional fluctuation or stress, we carried out both μ-PL and μ-Raman measurements at the same hillock on the $Al_xGa_{1-x}N$ film to study the influence of stress on the hillocks. The $Al_xGa_{1-x}N$ film was fixed on the glass slide for positioning the hillocks by using the scales of microscope, see Fig. 4-2-2. The step adjustment of movement is ~1 μm. In this study, we used μ-PL spectra to deduce the Al fraction across hillocks because PL results are relatively insensitive to the strain.

From the μ-PL spectra, the peak position can be converted into photon energy as :

$$E_g(eV) = \frac{1240}{\lambda(nm)}$$

By substituting it into the following empirical formula, one can obtain Al fraction ' x ' :

$$E_g^{Al_xGa_{1-x}N}(x) = E_g^{GaN}(1-x) + E_g^{AlN}x - bx(1-x)$$ (4-2-1)

where the following constants were used for calculation. [30]

Band gap of GaN : $E_g^{GaN} = 3.45(eV)$

Band gap of AlN : $E_g^{AlN} = 6.2(eV)$

Bowing parameter : $b = 1.3(eV)$

In order to study the influence of stress on hillocks, we applied the formula 4-2-1 to the μ-PL spectral peak to deduce the Al fraction of hillocks. Fig. 4-2-3 and Fig. 4-2-4 show the Al fraction distribution across 3μm mesa-like and 6μm tent-like hillocks, respectively. The Al fraction obtained from the EDX measurements agrees with that deduced from μ-PL spectra whether inside or outside hillocks.

Davydov et al. [31] reported that the E_2 phonon frequency increases monotonically with the Al fraction in $Al_xGa_{1-x}N$. According to their results, we can obtain the strain free E_2 phonon frequency for a given Al fraction, by substituting Al fraction into the following formula [31]:

$$E_2^{AlxGa_{1-x}N}(High) = E_2^{GaN}(1-x) + E_2^{AlN}x - b_{E_2(High)}x(1-x)$$ (4-2-2)

where

$E_2^{GaN}(High) = 567.4cm^{-1}$ is for strain free GaN ,

$E_2^{AlN}(High) = 609.2cm^{-1}$ strain free AlN , and

bowing parameter : $b_{E_2(High)} = 20cm^{-1}$

The strain free E_2 phonon frequency can be well fitted for the

composition range ($0 \leq x \leq 0.2$).

Then, by substituting the Al fraction from Figs. 4-2-3 and 4-2-4 into the formula 4-2-2, we obtain strain free E_2 phonon frequency for the same hillocks measured by μ-PL and μ-Raman scattering. By comparing the experimental E_2 phonon frequency to the strain free E_2 mode, the influence of stress on hillocks is revealed.
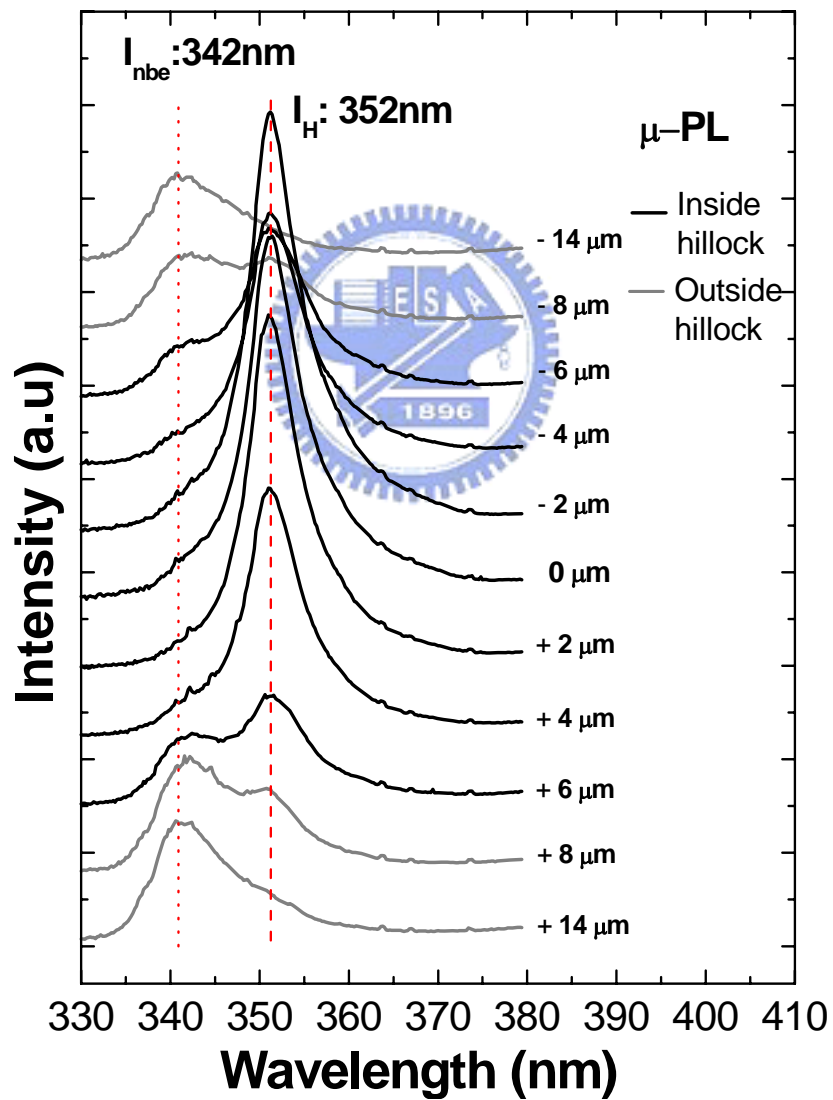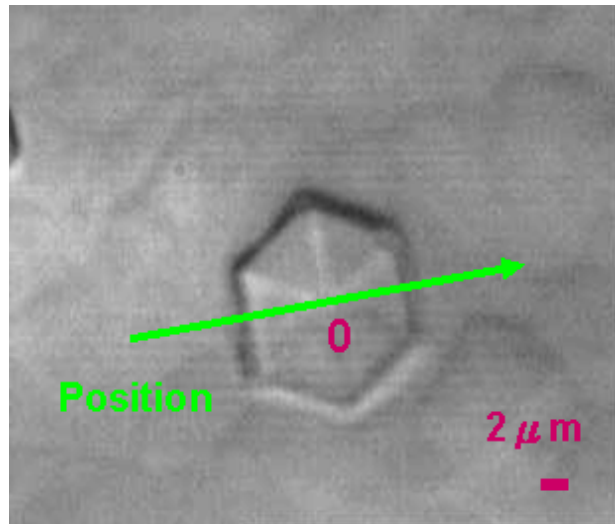
Fig. 4-2-1
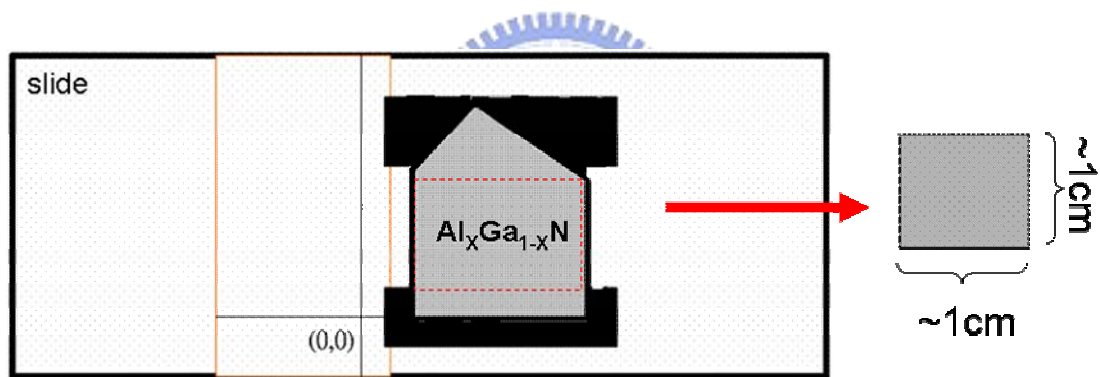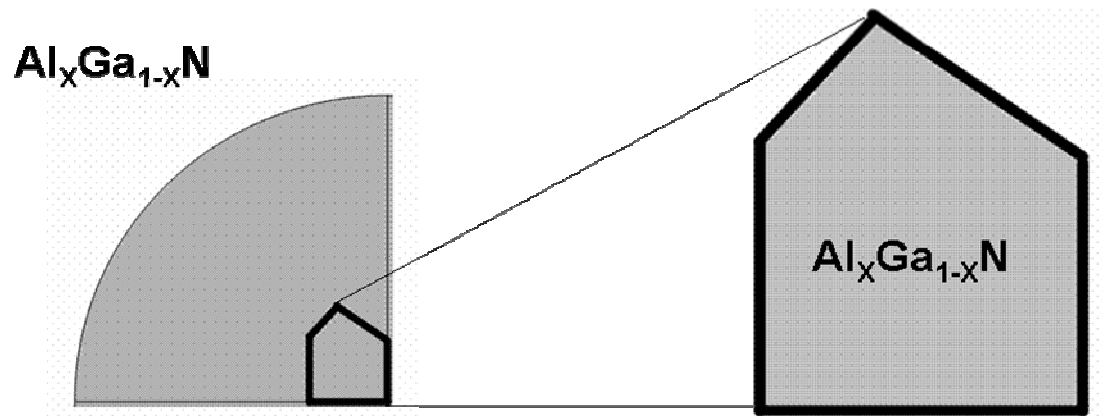
Fig. 4-2-2
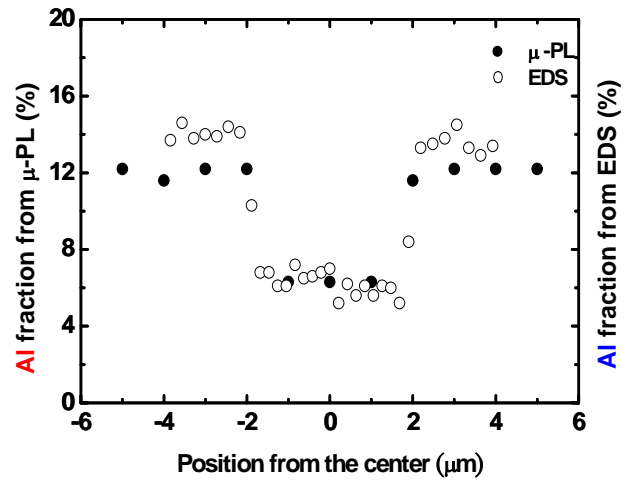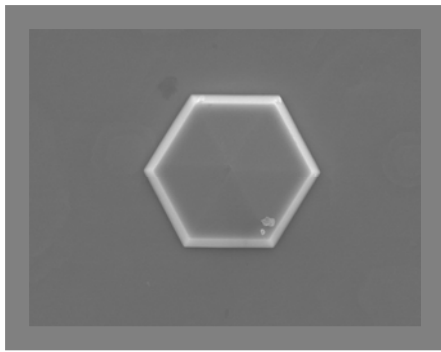
Fig. 4-2-3

Mesa-like hillock (3μm)
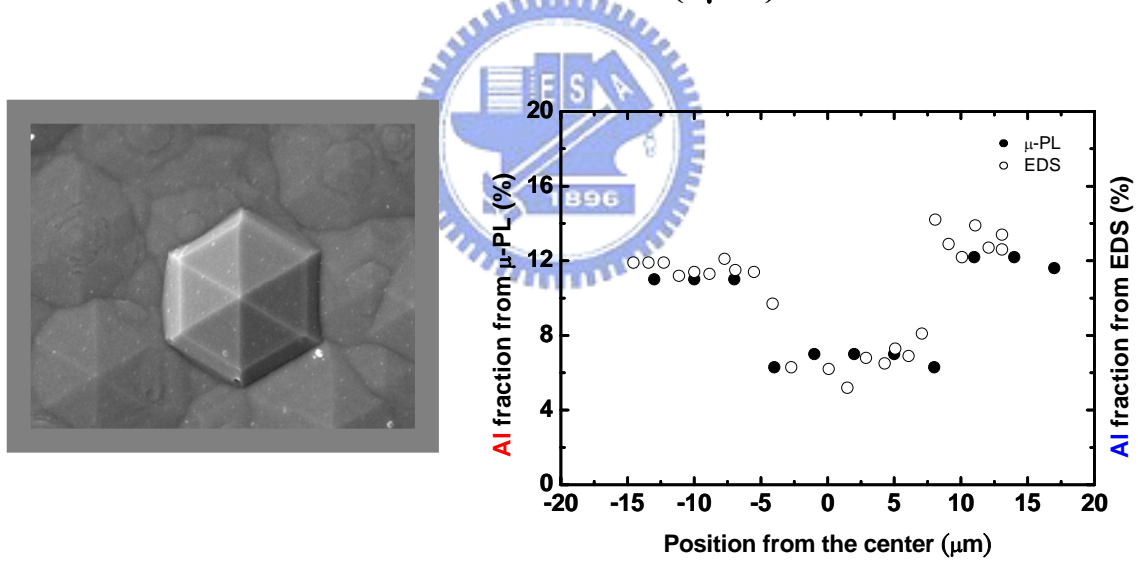
Fig. 4-2-4

Tent-like hillock (6μm)

4-3 The Micro-PL and Micro-Raman Spectra
of Tent-like Hillock

In order to investigate the effect of stress on the hillocks, we select a tent-like hillock with 10μm dimension (Fig. 4-3-1). From the μ-PL and μ-Raman spectra, the distinction between the inside and outside of the tent-like hillock is quite obvious.

As shown in Fig. 4-3-2 and Fig. 4-3-3, the μ-PL spectra of the tent-like hillock acquired at room temperature show the position-dependence with 0.2 nm resolution along the horizontal (non ridge line) and vertical (ridge line) line. The results show the I_{NBE} appearance at 342nm (3.625eV) outside the hillock. Besides, we also observe another emission peak at 353nm (3.512eV) and its intensity is stronger than the I_{NBE} from the outside region. In the previous study [29], we concluded that dissimilar peaks inside and outside the hillock are due to the Al variation. From the section 4-2, theoretical calculation of Al fraction through the results of μ-PL is very close to the EDX measurements. Thus, the EDX data also support with our interpretation of PL emission origin.

Since the optical properties of hillocks are dominated by the Al fraction fluctuation, we chose the μ-PL peak position to estimate the Al fraction in the probed region by substituting the peak energy into the formula 4-2-1. Fig. 4-3-4 (a) and Fig. 4-3-4 (b) show the corresponding

Al fraction that is about 4% and 11% inside and outside the hillock, respectively. Then, we adopted the Al fraction and applied the formula 4-2-2 (section 4-2) to calculate the strain free E_2 mode frequency of this 10μm hillock which is ~568.5 cm^{-1} inside the hillock and ~570 cm^{-1} outside the hillock as shown by the dashed lines in Fig. 4-3-5 (a) and Fig. 4-3-5 (b).

In addition to μ-PL spectra, we also used μ-Raman scattering to investigate the E_2 modes of the same 10μm tent-like hillock in order to estimate the strain relaxation between the hillock and surroundings. The μ-Raman spectra were measured at room temperature with ~0.5 cm^{-1} resolution. Fig. 4-3-6 shows the six scan directions on the tent-like hillock, in which lines 1, 3, 5 focus on the ridge and lines 2, 4, 6 focus on non-ridge. As shown in Fig. 4-3-7, the E_2 mode frequency is ~573 cm^{-1} outside the tent-like hillock, but shifts toward ~570 cm^{-1} inside the hillock. The six line scans have the similar Raman distribution inside the tent-like hillock, except ~1cm^{-1} larger shift at the apex.

The μ-PL results showed that the peak positions inside the hillock are all near 353nm and the fluctuation is less than 1nm. According to the formula 4-2-1 and 4-2-2, the 1nm fluctuation is corresponding to 0.66% of Al fraction, and this will cause only 0.17 cm^{-1} difference in E_2 mode frequency. However we served ~1 cm^{-1} difference between apex and sidewall. If the ~1 cm^{-1} difference is caused by the Al fraction, it would mean ~3.73% Al deviation from the hillock center to edge, and then μ-PL

spectra will have 5.6nm wavelength shift across the hillock. Thus, the ~1cm^{-1} deviation from the apex to its surroundings can not be caused by Al fluctuation, but by the stress.

Furthermore, the fluctuation of the E_2 mode frequency outside this hillock may be attributed to the influence of the A-type hillocks which spread extensively on the sample.

In order to expose the influence of stress on tent-like hillocks, we compare the strain free E_2 mode frequency obtained from Al fraction with the experimental Raman results as shown in Fig. 4-3-8. The Raman E_2 mode shift deviation is ~1.5 cm^{-1} and ~3 cm^{-1} inside and outside the tent-like hillock respectively. They are blue-shifted implying that the outside of hillock bears much larger compressive stress than the hillock itself, and the hillock apex also bears larger stress than its surroundings. The compressive stress is estimated to be 0.3 GPa and 0.7 GPa inside and outside the tent-like hillock, respectively[32].

On the other hand, the full width at half maximum (FWHM) of μ-PL and μ-Raman scattering of this tent-like hillock are shown in Fig. 4-3-9 (a) and Fig. 4-3-9 (b) for horizontal and vertical line scans. It is obvious that the FWHM inside the hillock is narrower than that outside the hillock and it decreases gradually to the hillock center by 25meV and 3.5 cm^{-1}. In Fig.4-3-10 (a) and 4-3-10 (b), the μ-PL and μ-Raman scattering show much stronger intensity inside the hillock than that outside the hillock by a factor of 5-6. From our results, hillock is considered a good light

emission structure.

In the next section, the stress influence on various sizes of tent-like hillock will be discussed.

Tent-type Hillock

10um
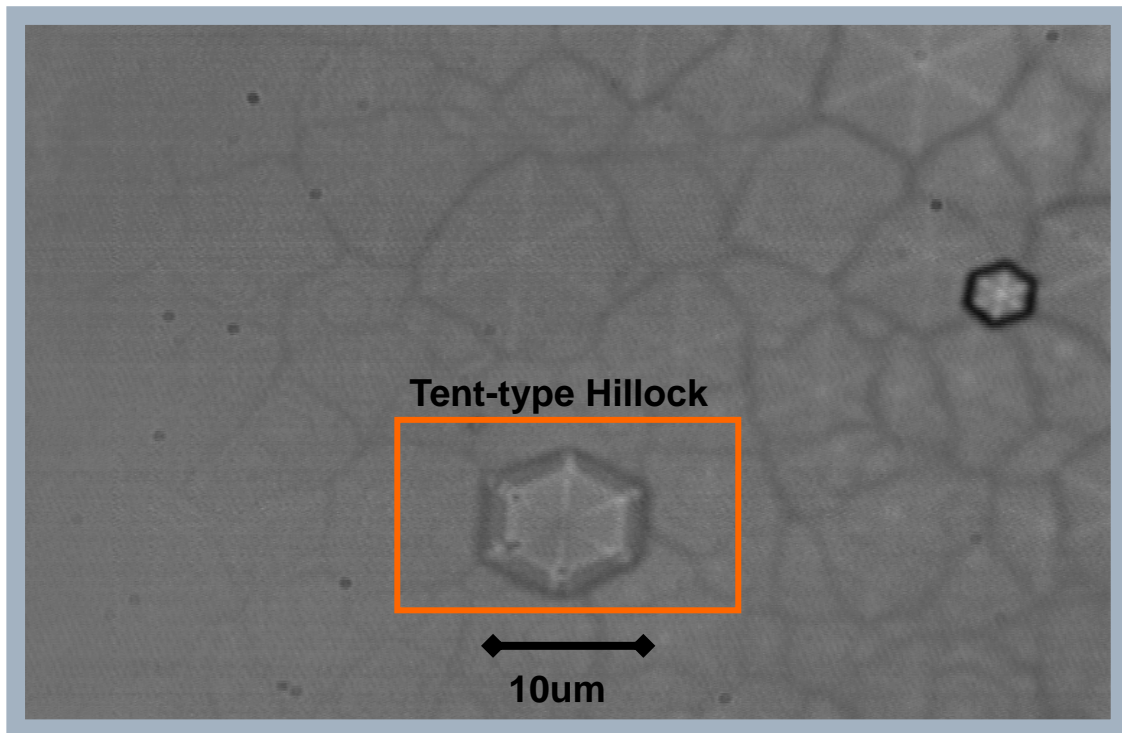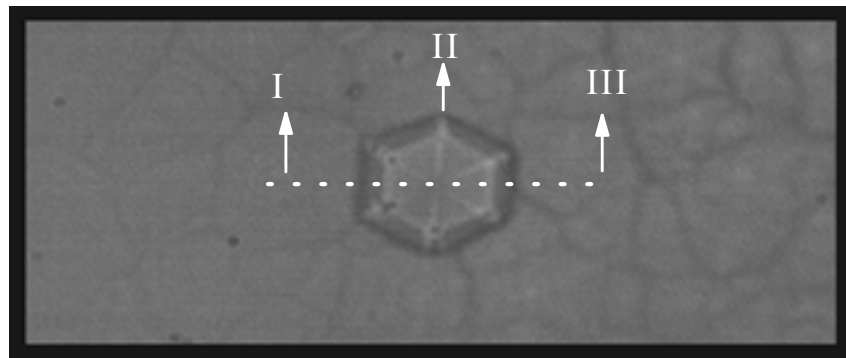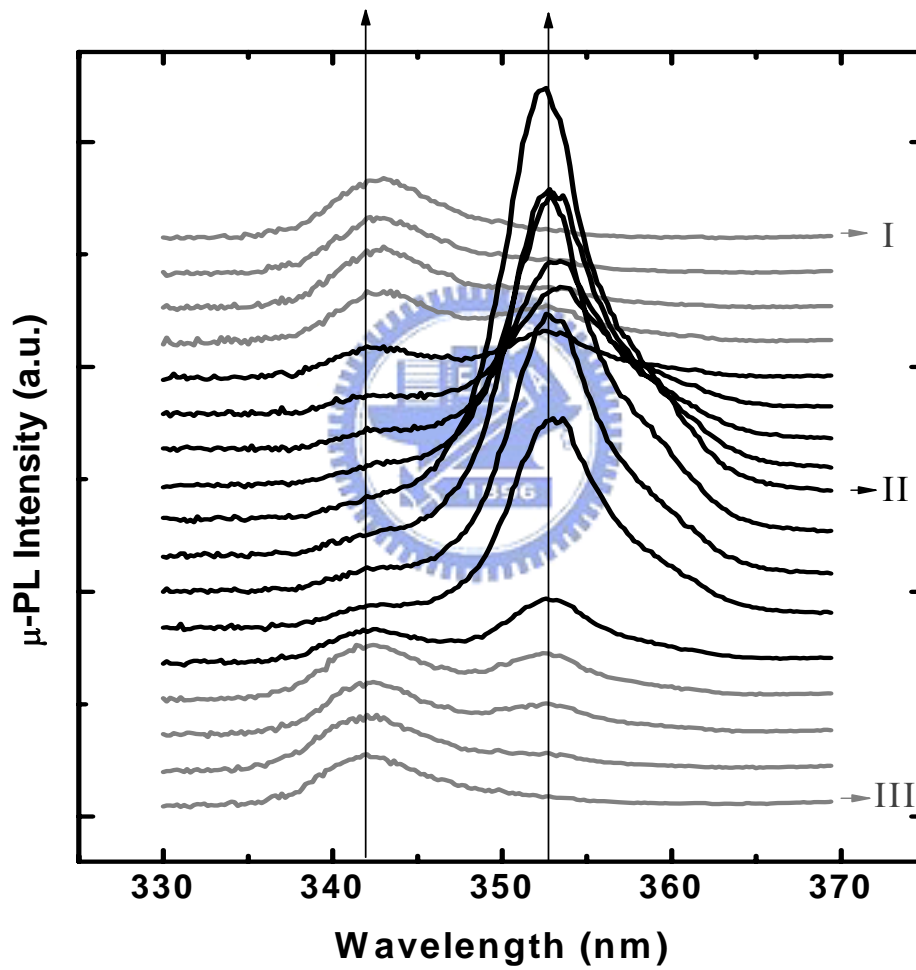
Fig. 4-3-1

Fig. 4-3-2

Horizontal line scan.

Optical image and spatially resolved μ-PL spectra of tent-type hillock.
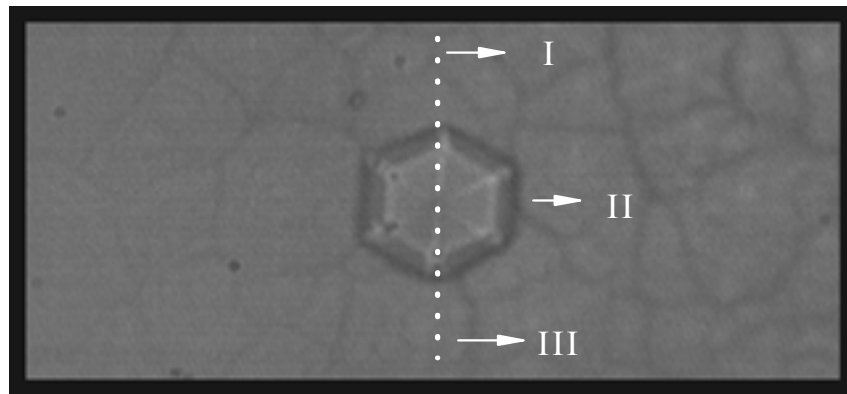
~342nm   ~353.3nm
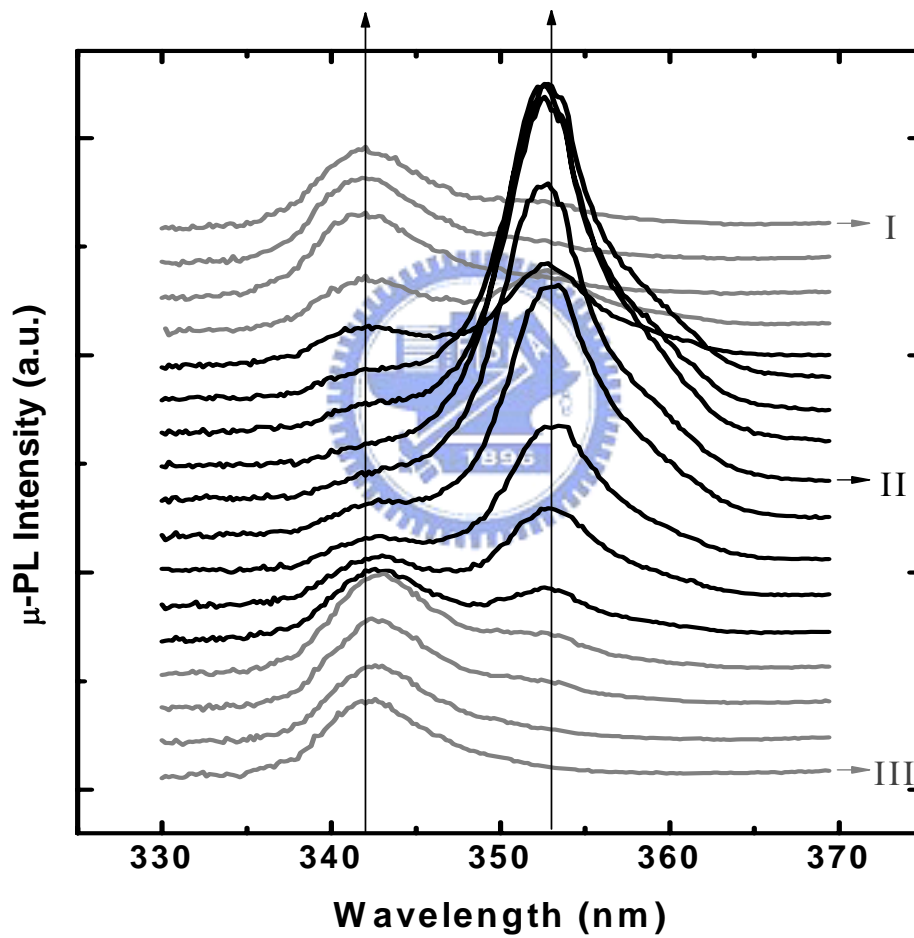
Fig. 4-3-3

Vertical line scan.

Optical image and spatially resolved μ-PL spectra of tent-type hillock.
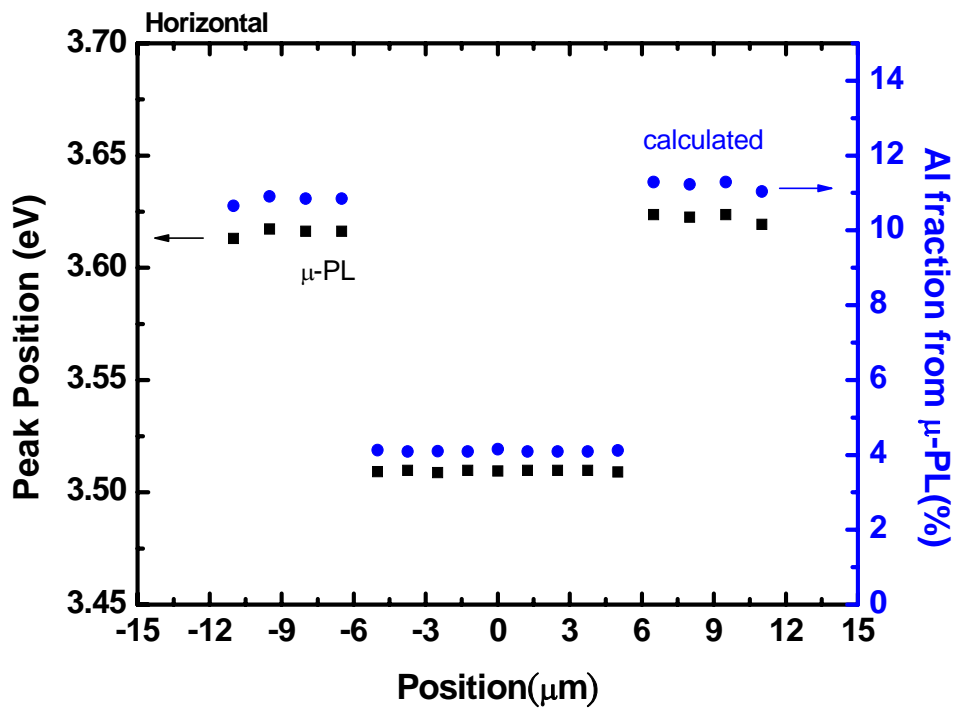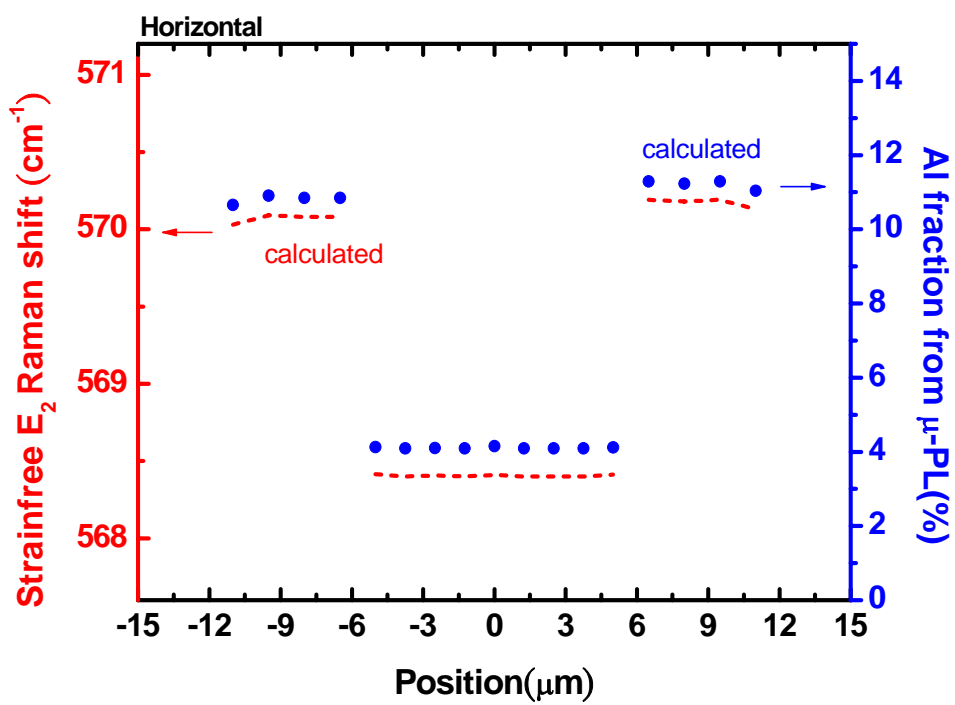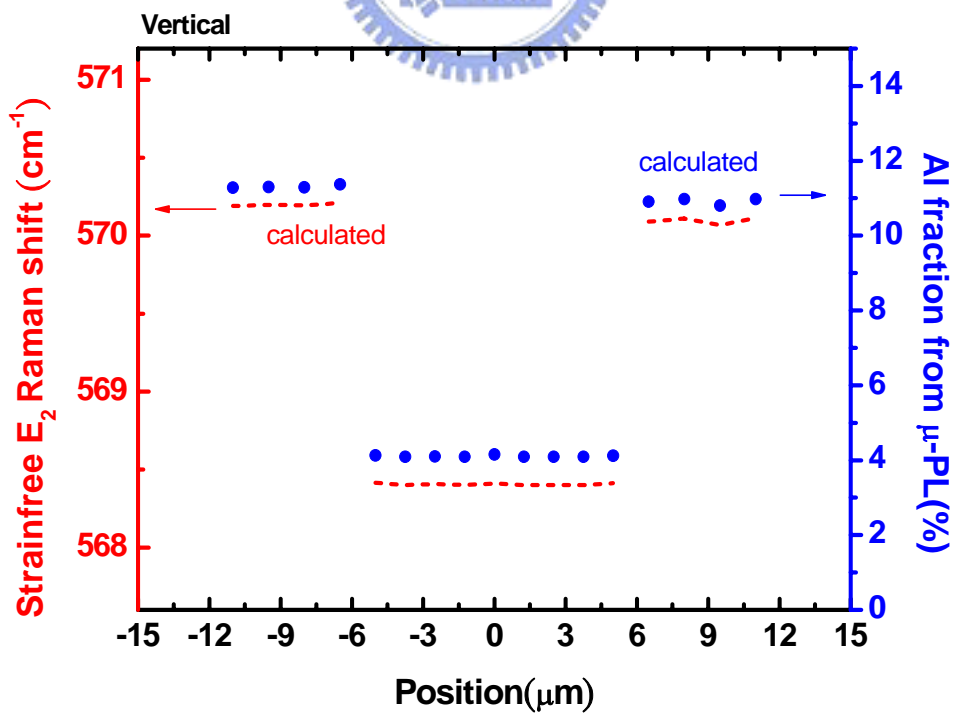
Fig. 4-3-4 (a)
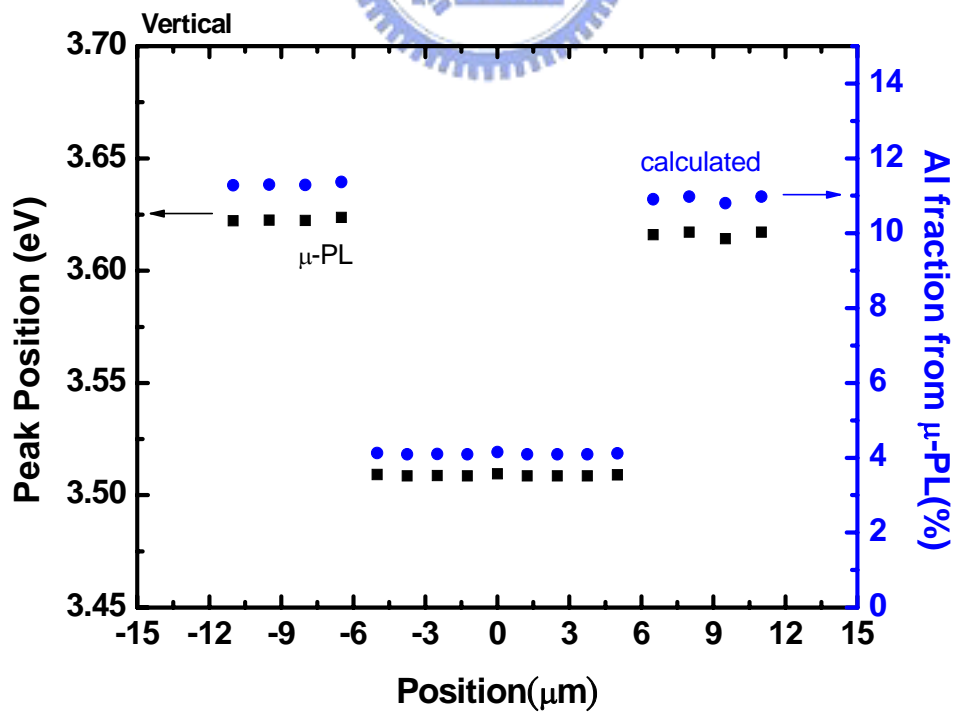
Fig. 4-3-4 (b)

Fig. 4-3-5 (a)

Fig. 4-3-5 (b)

Tent-like Hillock : 10μm

Line 1

Line 3

Line 5

Line 2

Line 4

Line 6
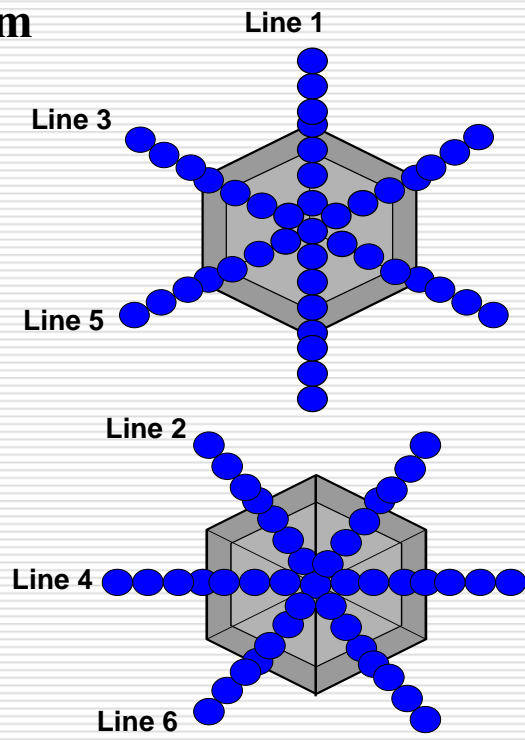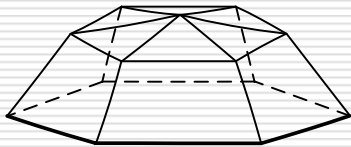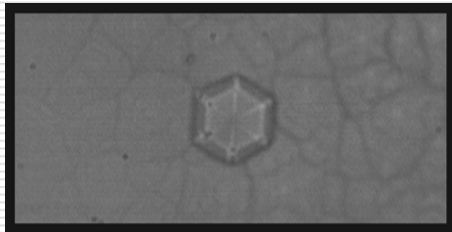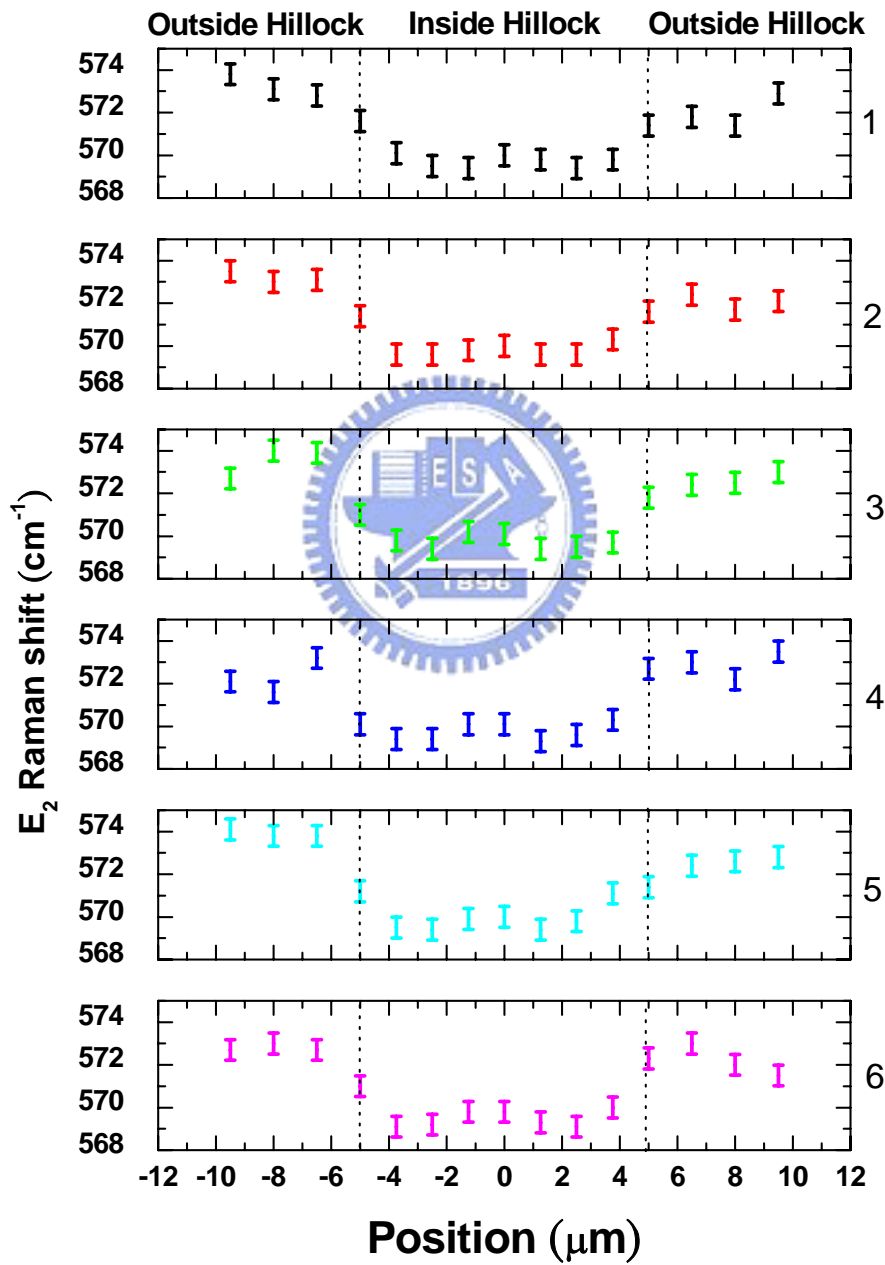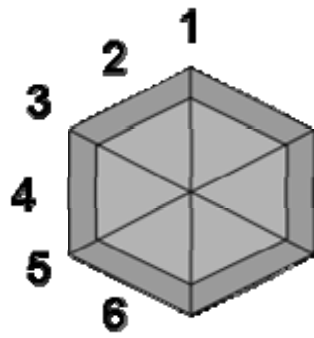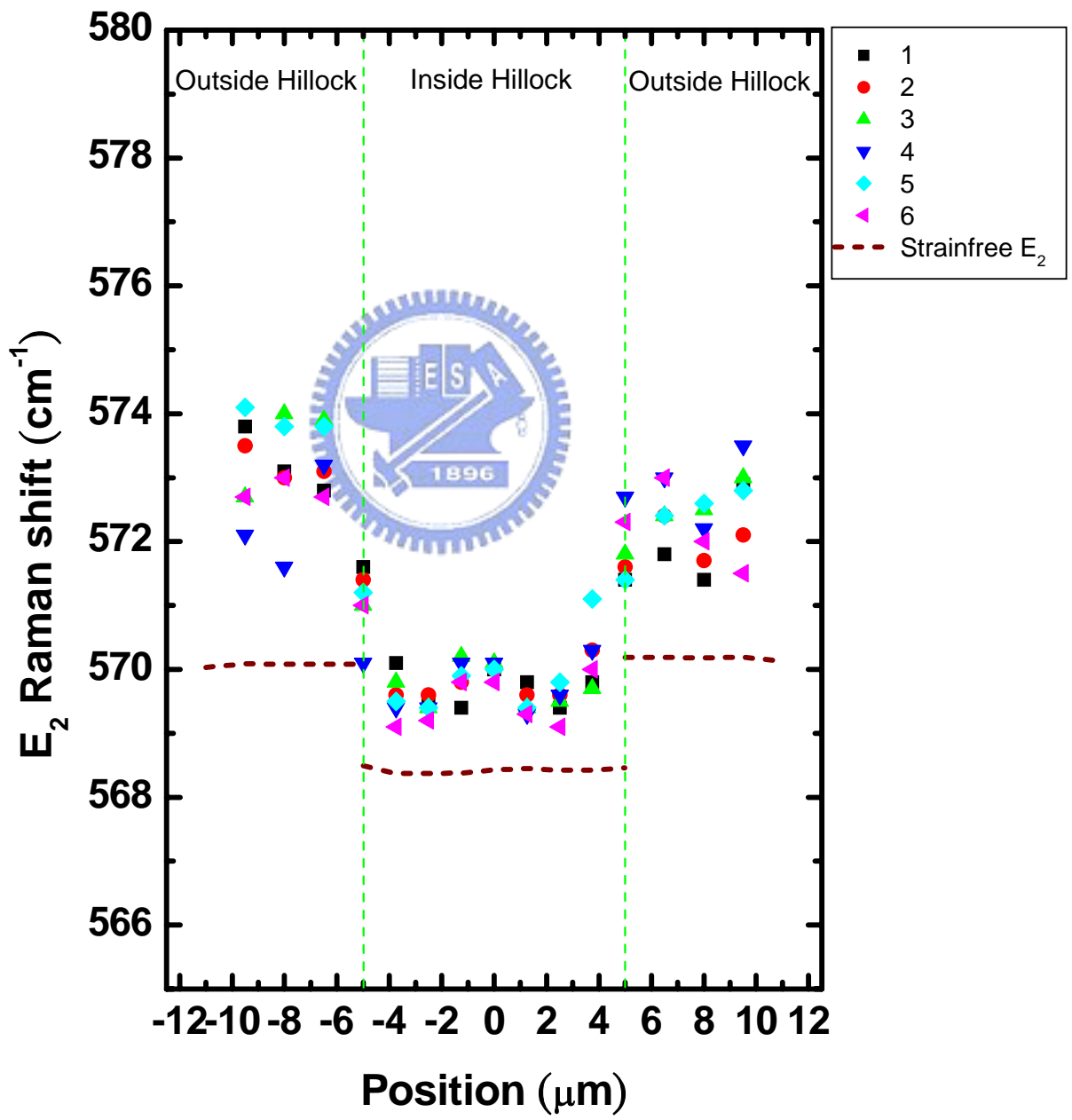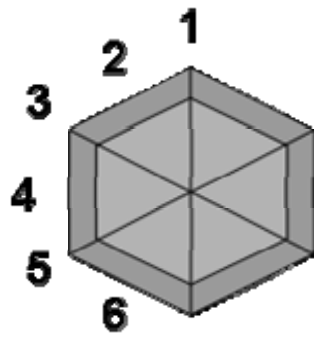
Fig. 4-3-6
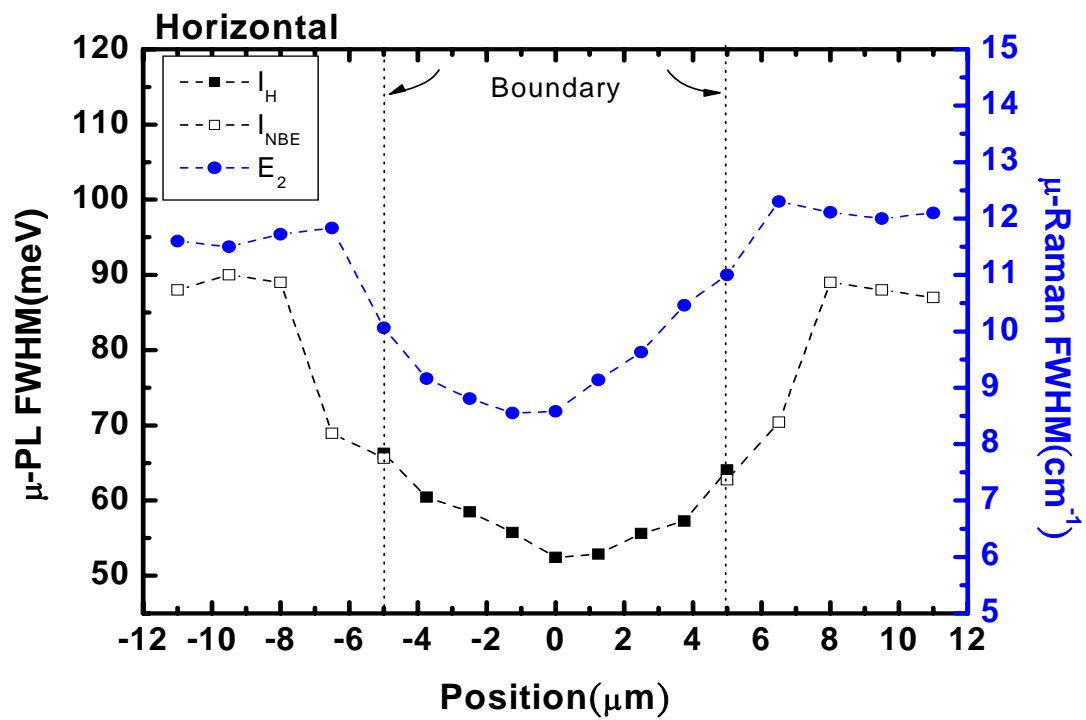
Fig. 4-3-7

Fig. 4-3-8

Fig. 4-3-9 (a)
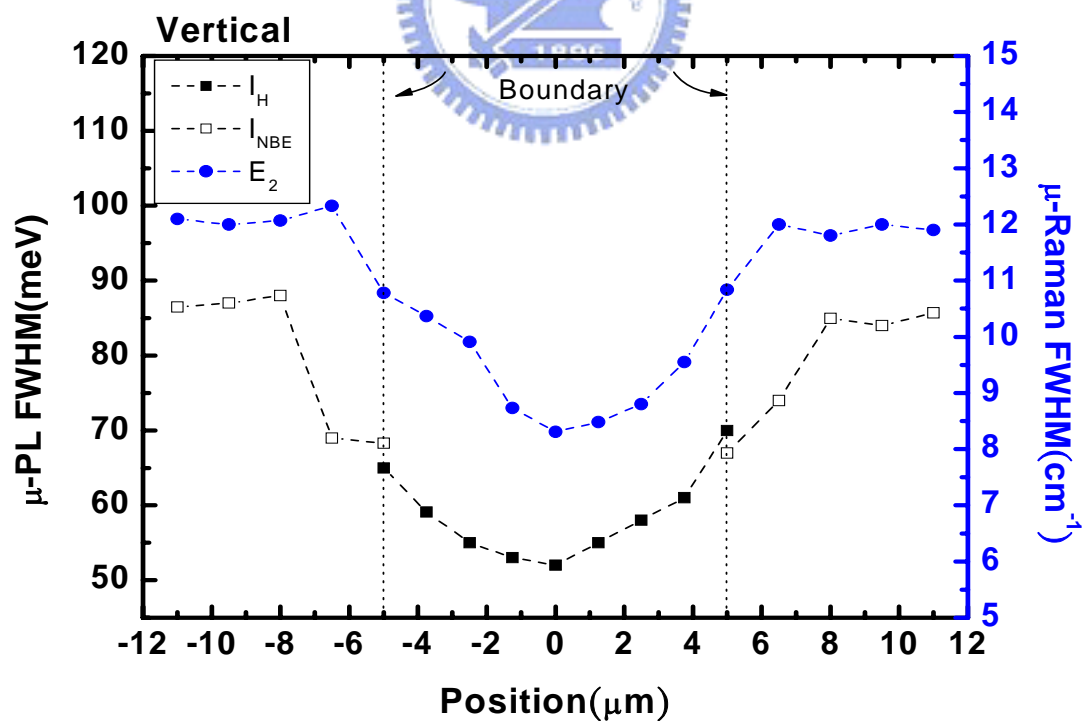
Fig. 4-3-9 (b)
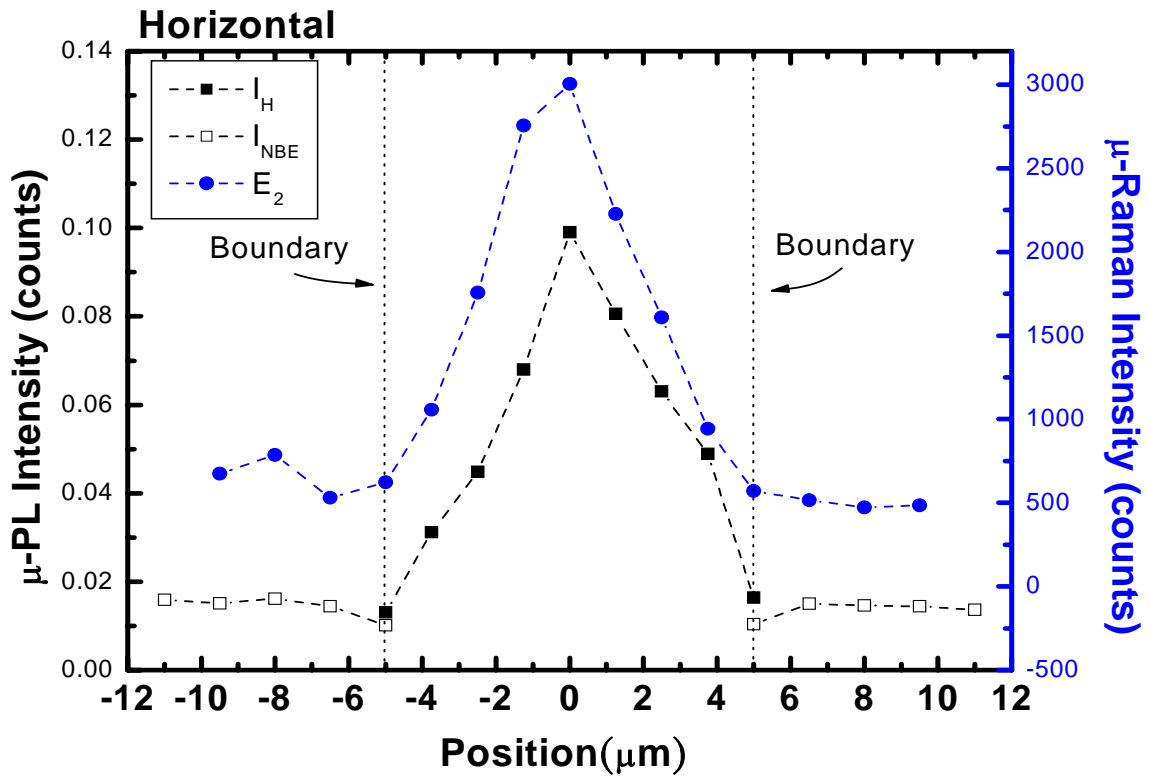
Fig. 4-3-10 (a)
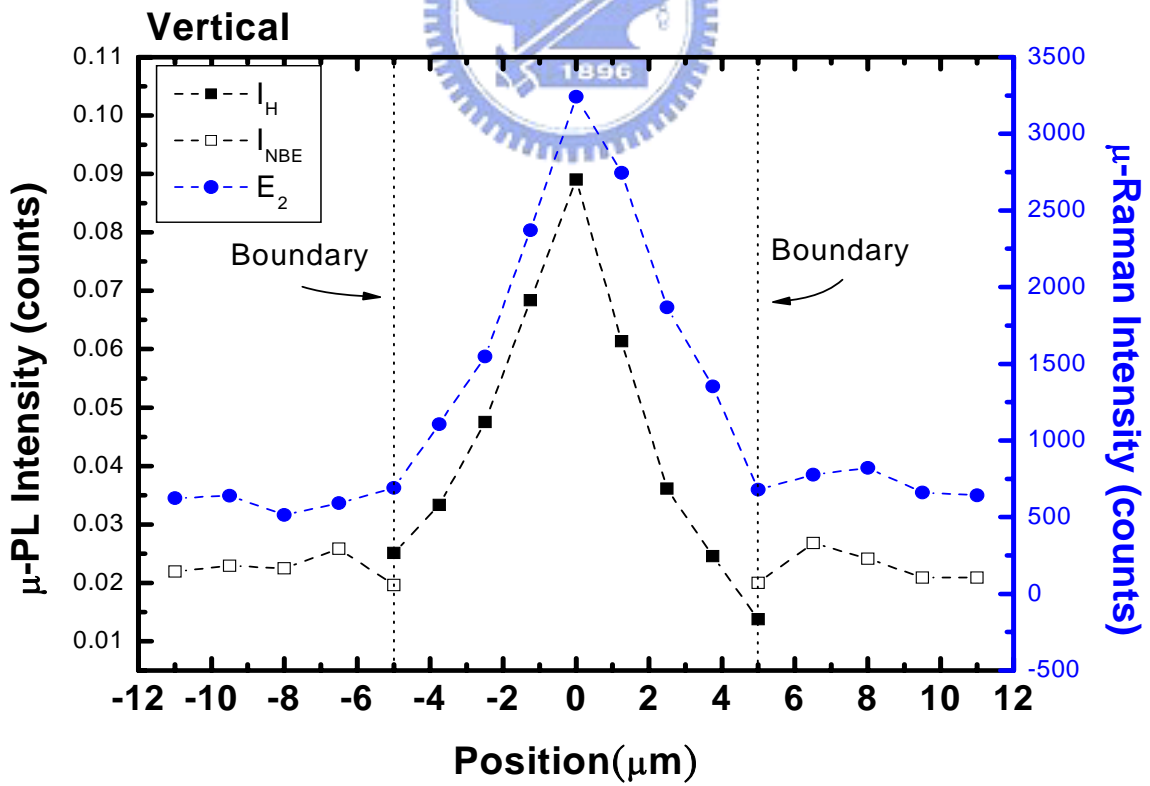
Fig. 4-3-10 (b)

4-4   The Size-Dependence Micro-PL and Micro -Raman of Tent-like Hillock

Previously, the spatially resolved μ-PL and the μ-Raman spectra of the tent-like hillock with 10 μm size were analyzed to elucidate the photo-carriers recombination process and the phonon behavior. The results showed that the compressive stress occurred both inside and outside the hillock with its apex experiencing higher stress than sidewall. In this section, we want to study the stress influence on different sized hillocks in $Al_xGa_{1-x}N$ film.

As shown in Fig.4-4-1 the diameter of hillocks are ranged from 3 to 11 μm in which only 3, 4, and 5 μm are mesa-like hillock; others are tent-like hillock. Fig. 4-4-2 shows their μ-PL spectra at the hillock apex. The peak position is red shifted by 3.1 nm from 6 to 11μm of these tent-like hillocks. This phenomenon is consistent with the previous work by Chen *et al.* [1]. The Al fraction estimated from μ-PL peak position for various sized hillocks is shown in Fig. 4-4-3. Since I_{NBE} is at 342nm (3.625eV) outside all the hillocks, the Al fraction is about 11%. By increasing the size from 6μm to 11 μm, the red shift is from 65 to 115meV. This indicates that the Al fraction decreases progressively while the hillock size increases. The Al variation is about 2% in these tent-like hillocks. In contrast, the mesa-like hillocks have counter behavior with respect to the tent-like hillocks by showing the blue shift and the Al fraction increases with the increasing hillock size.

The μ-Raman scattering was also performed at the apex of this series hillocks as shown in Fig. 4-4-4 of spectra. Combining the results of the

μ-PL and μ-Raman scattering in Fig. 4-4-5, the Al fraction is obtained from μ-PL spectra and strain free E_2 mode frequency is calculated. The difference between strain free E_2 and experimental E_2 mode frequency is clearly observed in all hillocks. For the tent-like hillocks, as the size increases, the stress also increases. For the mesa-like hillocks, a counter behavior appears that the stress decreases as the size increases.

By focusing on the tent-like hillocks, we collected the spatially resolved Raman data in Fig. 4-4-6 to analyze the distribution of the E_2 mode frequency. The E_2 mode frequency is ~570 cm^{-1} inside each hillock, and ~573 cm^{-1} outside the hillock. Apparently, all these hillocks have the same distribution of the E_2 mode frequency as shown in the Fig.4-4-7 except the different sizes.

From the μ-PL and μ-Raman spectra, we found that all the hillocks, whether mesa-like hillocks or tent-like, bear the compressive stress. Einfeldt *et al*. [33][34] and Rudloff *et al*. [35], pointed out that AlGaN layer grown on GaN/sapphire formed the cracks to release the tensile strain. In our sample, the AlGaN layer grown on AlN buffer/sapphire, the formation of hillocks bears less compressive stress than the surroundings suggesting part of the stress is released by the protrusion of hillocks.
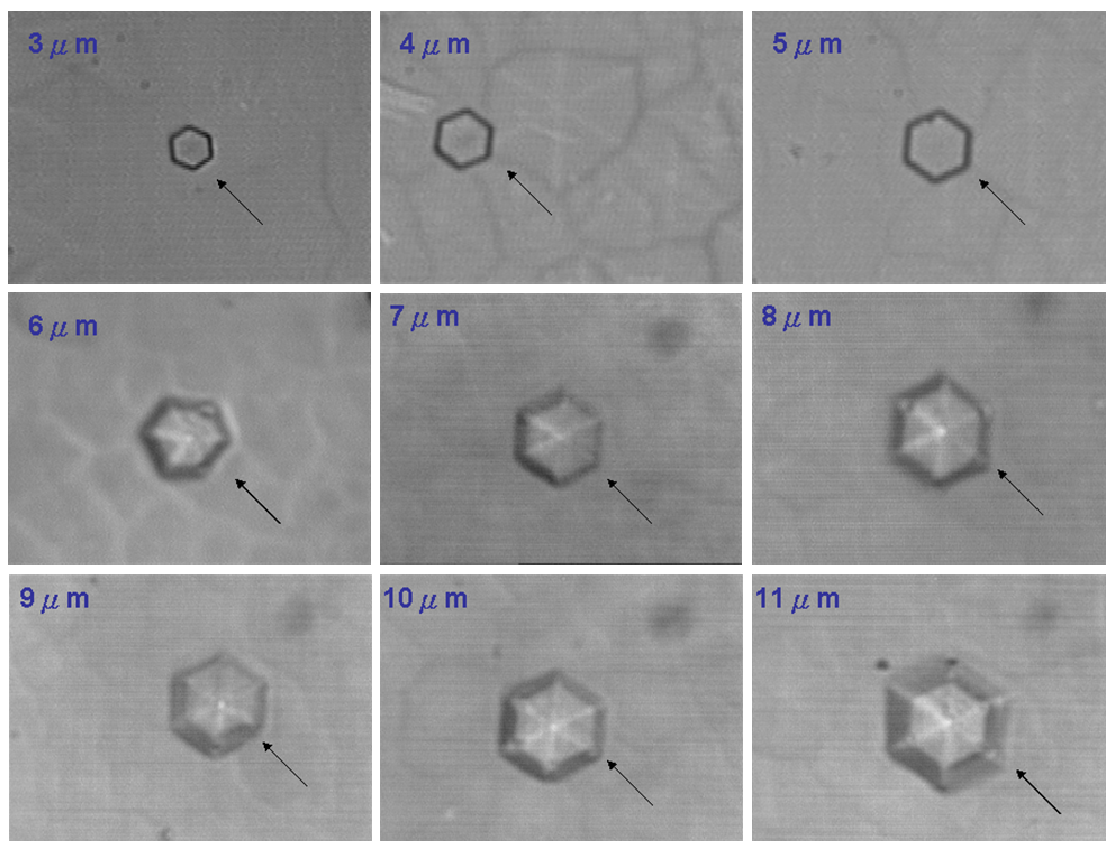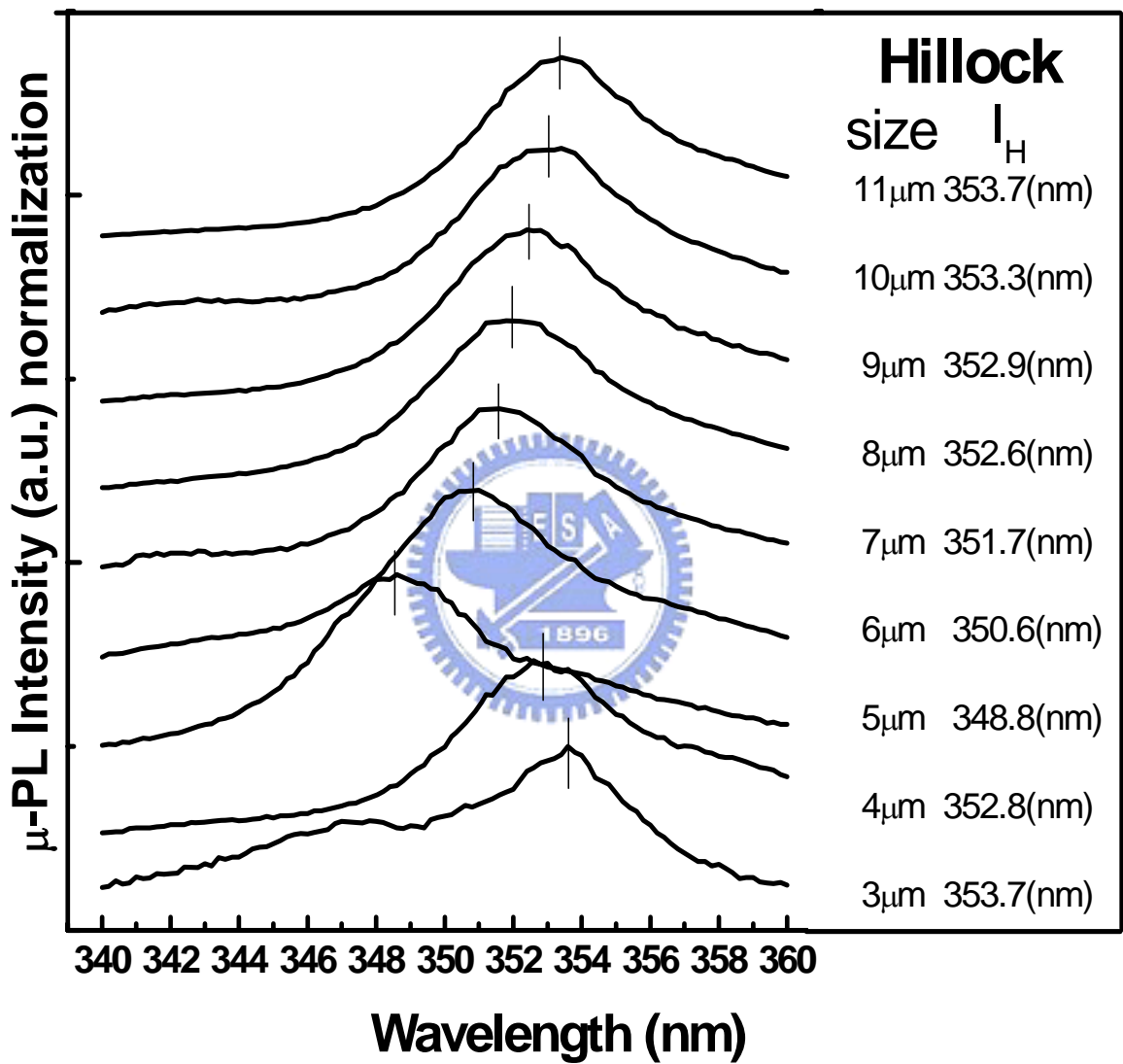
Fig. 4-4-1
Size：3 μm ~ 11μm

Fig. 4-4-2
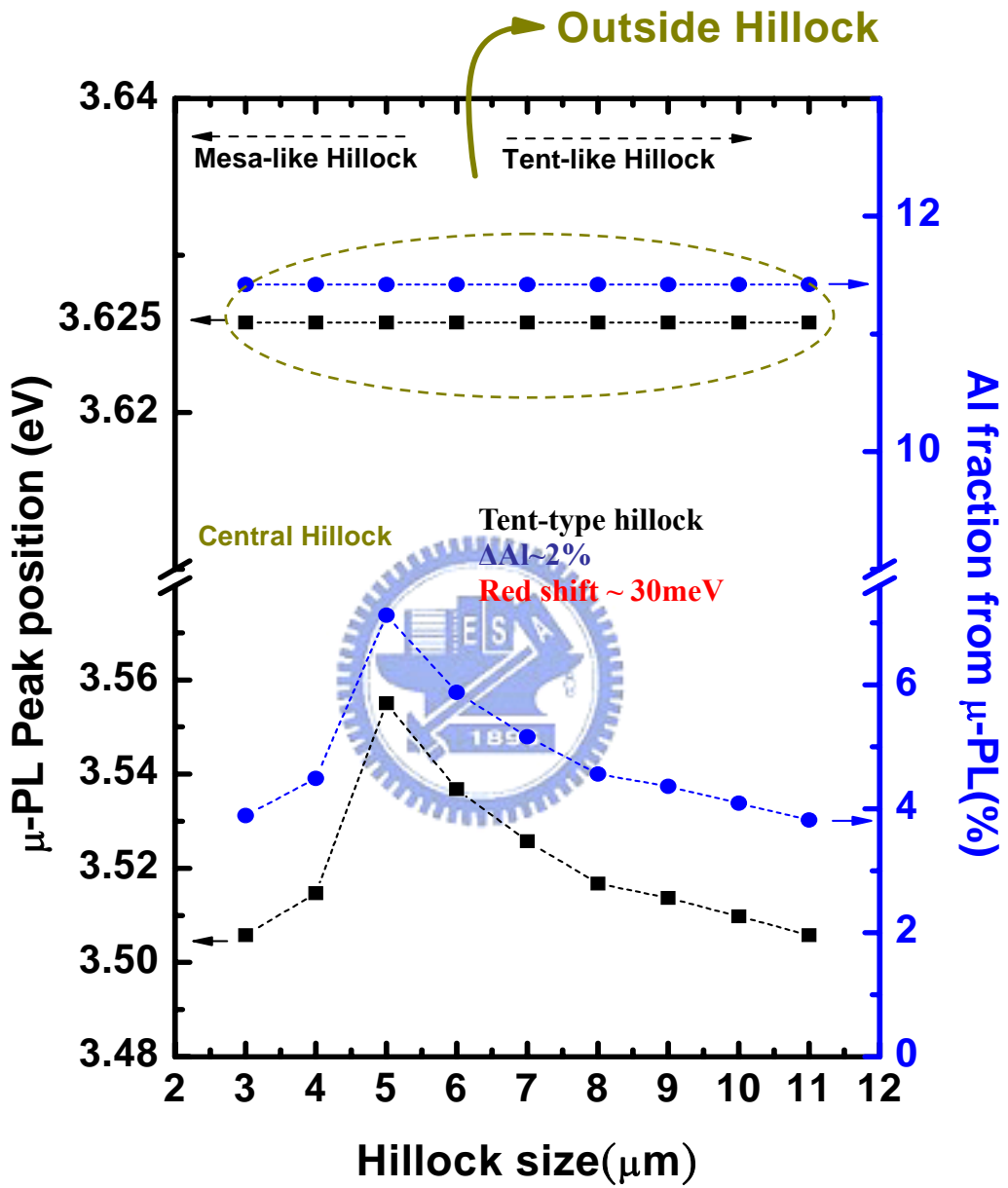**The μ-PL spectra of different size hillocks**
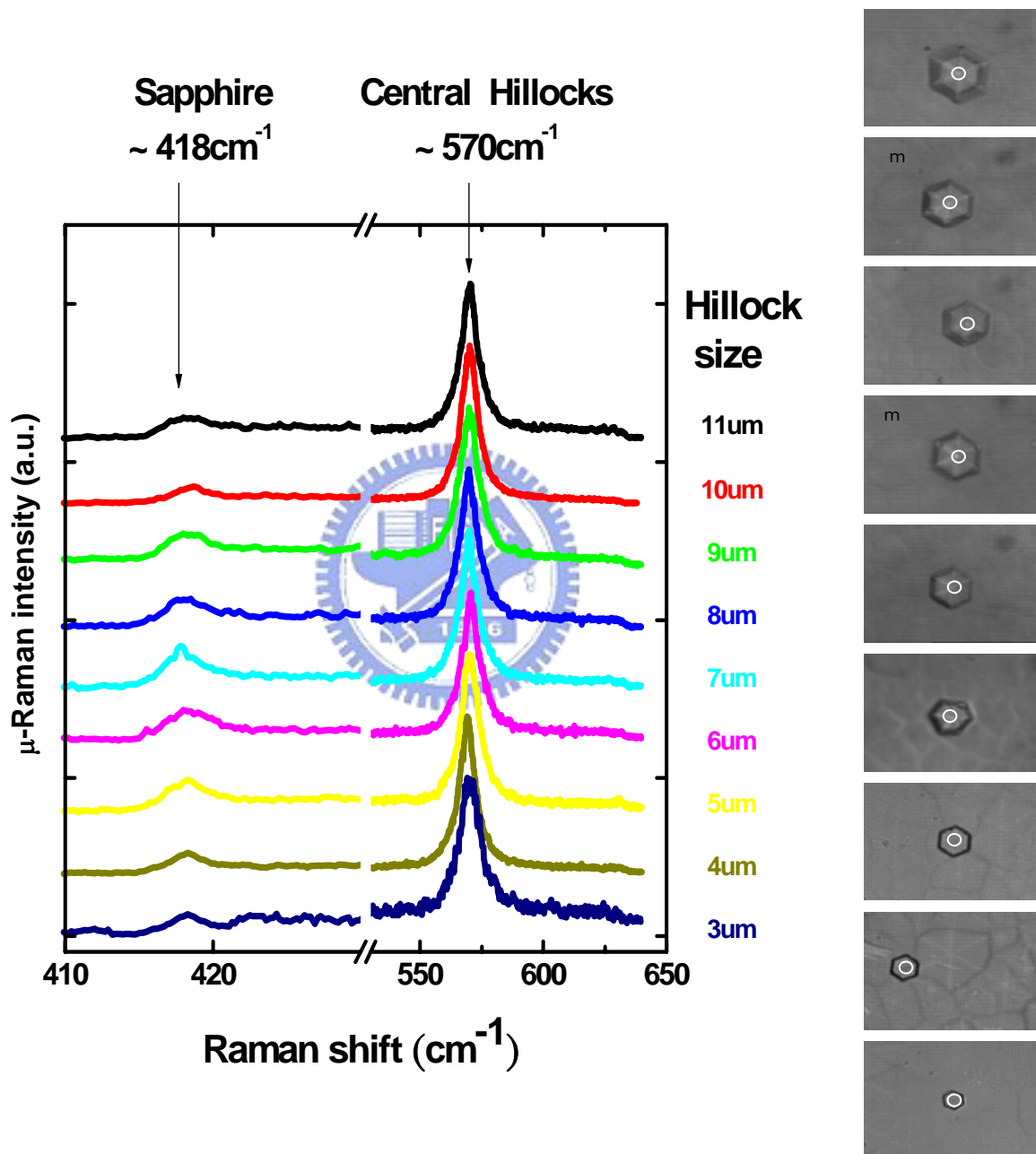
Fig. 4-4-3
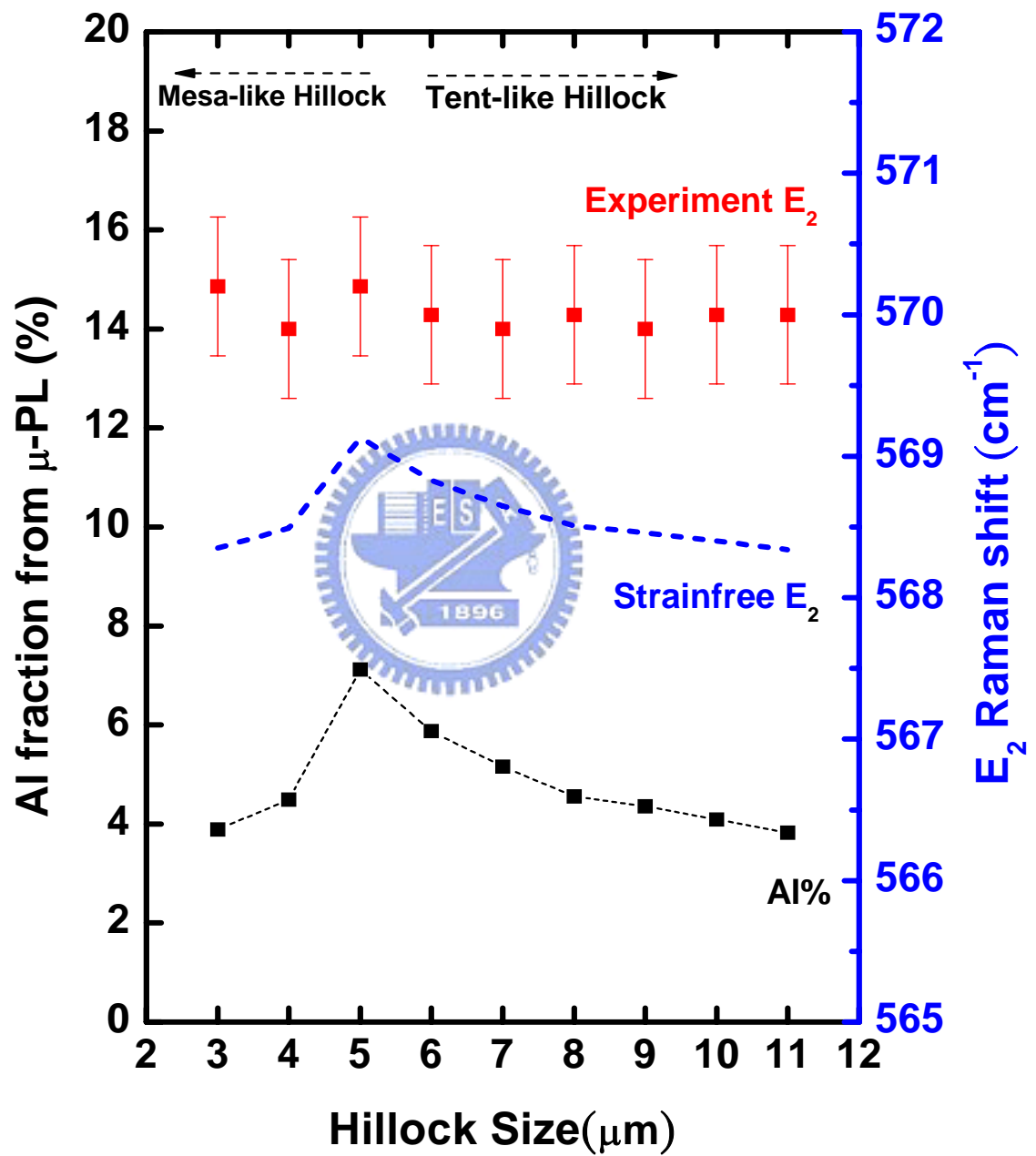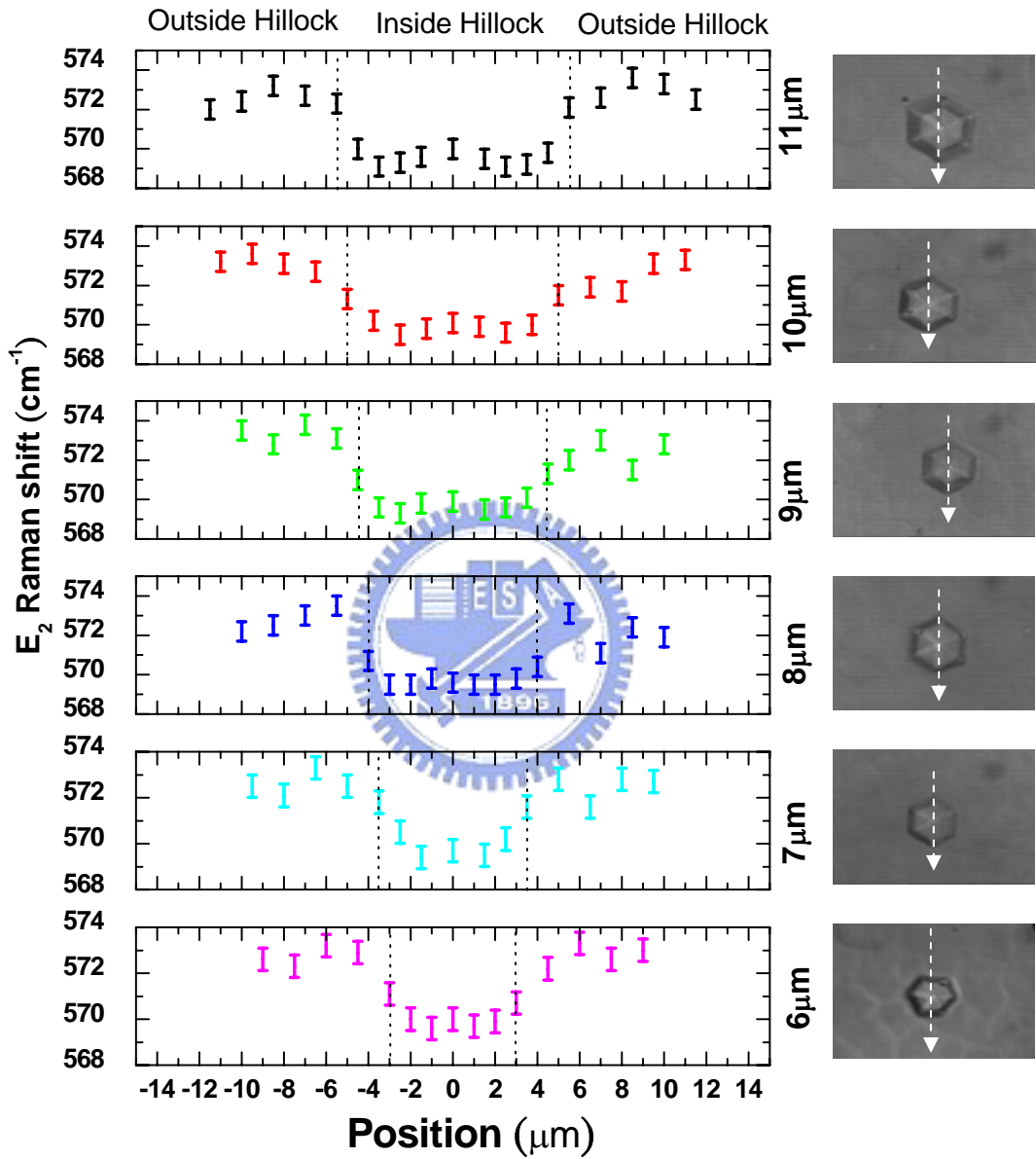
Fig. 4-4-4

Fig. 4-4-5

Fig. 4-4-6
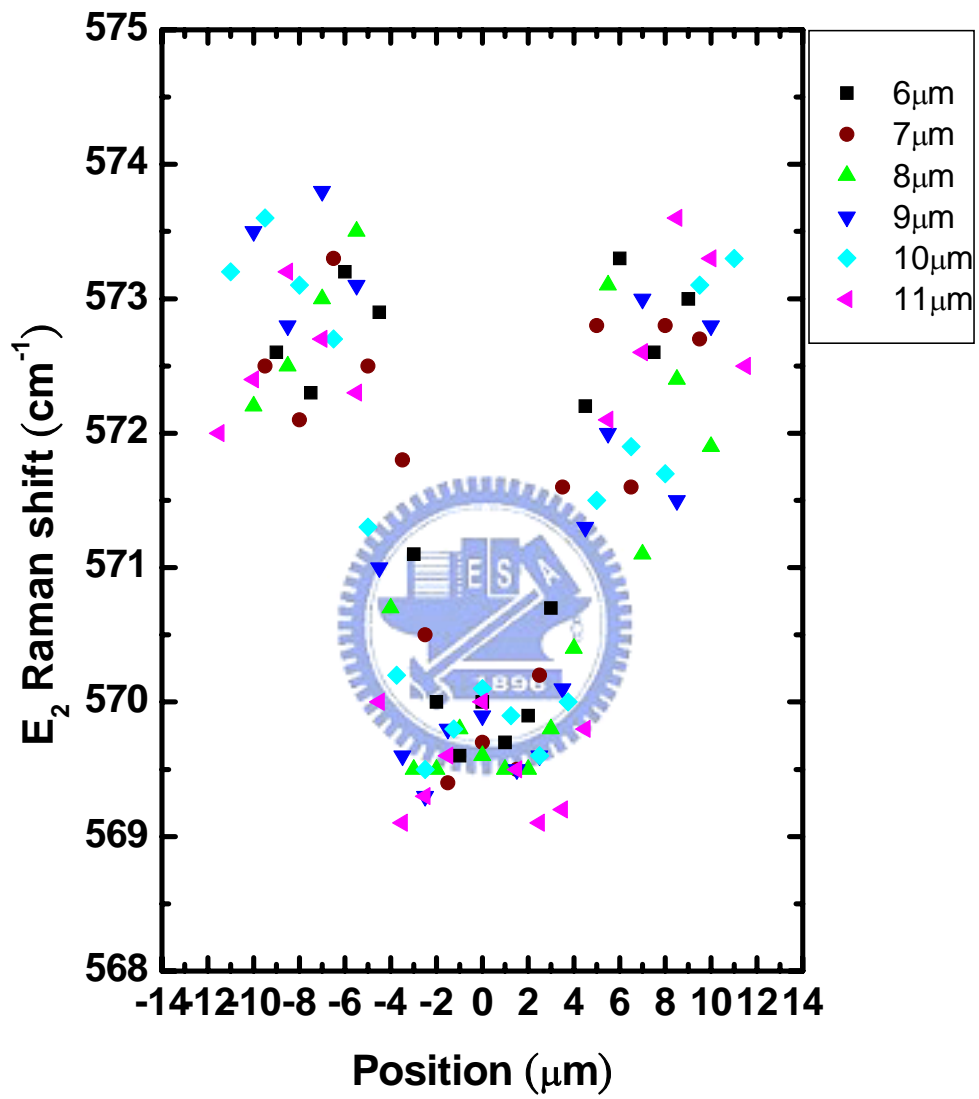**Size-dependent E$_2$ Raman mode of tent-like hillocks**

Fig. 4-4-7

4-5　Depth Analysis of Tent-like Hillock

There are two possible kinds of hillocks formation, the first one is that hillocks grow on the surface as shown in Fig. 4-5-1(a); the second one is that hillocks start to grow from the AlN buffer as shown in Fig. 4-5-1(b). From the previous section, the E_2 mode frequency is ~570 cm^{-1} inside hillocks and ~574 cm^{-1} outside hillocks. By depth probing, one does expect the presumed Raman distributions for either case in Fig. 4-5-1.

To investigate how deep hillocks are formed, we moved the probe focus at different depths into the 10μm tent-like hillock. The laser spot was first focused on the surface through the microscope. Then focusing was adjusted by 1μm step from the surface to the bottom. The confocal hole aperture was set at 900μm and the range of focal depth was about 3μm.

On the central tent-like hillock, its Raman spectra at different depths are shown in Fig. 4-5-2(a). The E_2 mode frequency remains at ~570 cm^{-1}, and it does not shift while the focus depth increases. However, the sapphire E_2 mode intensity at 577 cm^{-1} [36] grows obviously with the increasing focus depth as shown in an enlarged view of Fig. 4-5-2(b).

To compare with the tent-like hillock behavior, we also studied the A type hillock just outside this tent-like hillock. As shown in Fig. 4-5-3(a), the E_2 mode frequency of A type hillock is fixed at ~574 cm^{-1}, and it does not shift with the increasing focus depth either, in spite of the sapphire signals at 577 cm^{-1} that become even stronger as shown in Fig. 4-5-3(b).

The experimental data are collected in Fig. 4-5-4 for comparison.

According to the depth analysis of tent-like hillock, it is evident that the formation of hillock is from the AlN buffer layer, in consistent with the assumption of Fig. 4-5-1(b). It is likely that hillock position is determined by the AlN buffer grown on sapphire. When $Al_XGa_{1-X}N$ is deposited on the AlN buffer, hillocks are then formed spontaneously by balancing and reducing the internal strain of the sample film[37].
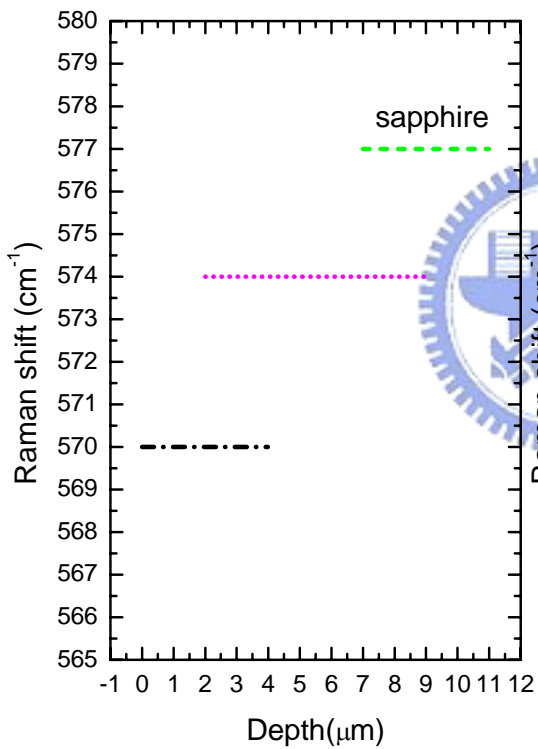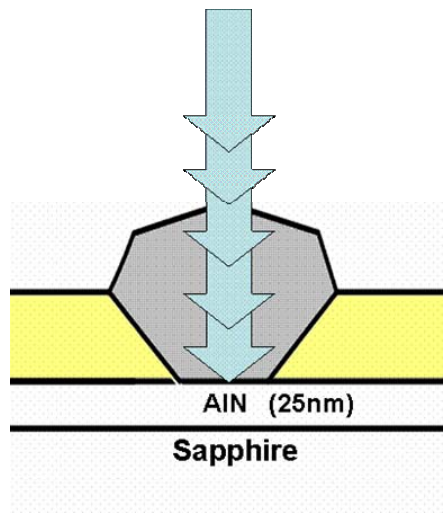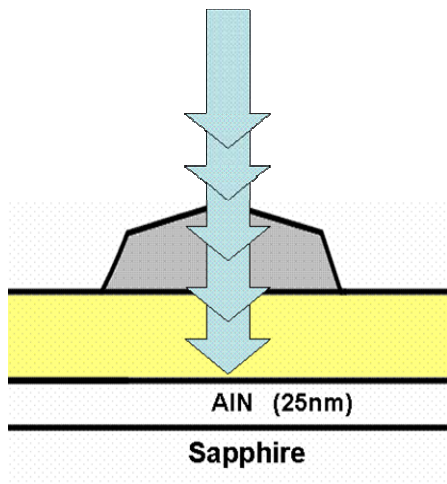
4-5-1 (a)

Hillocks grow on the surface
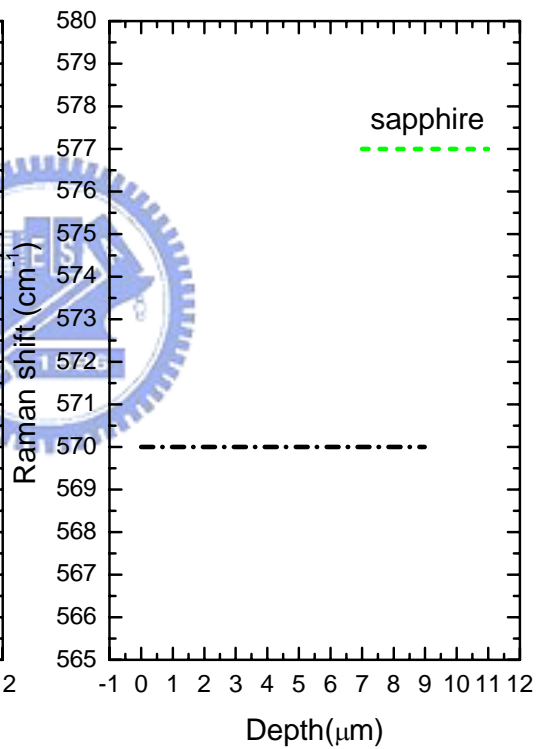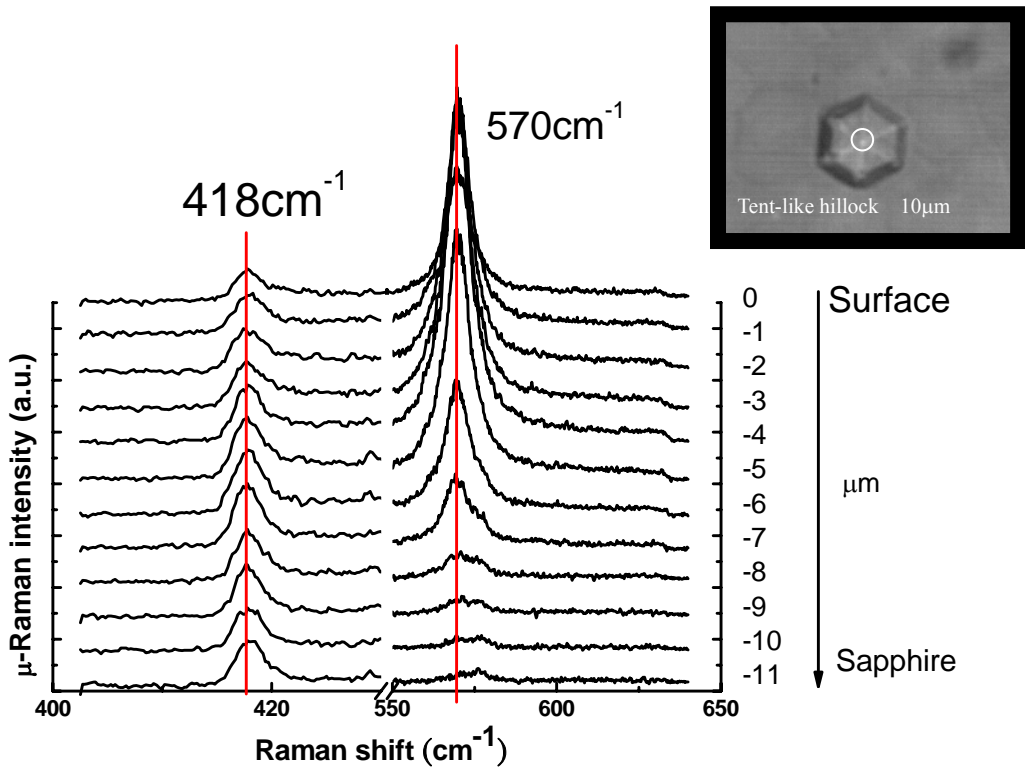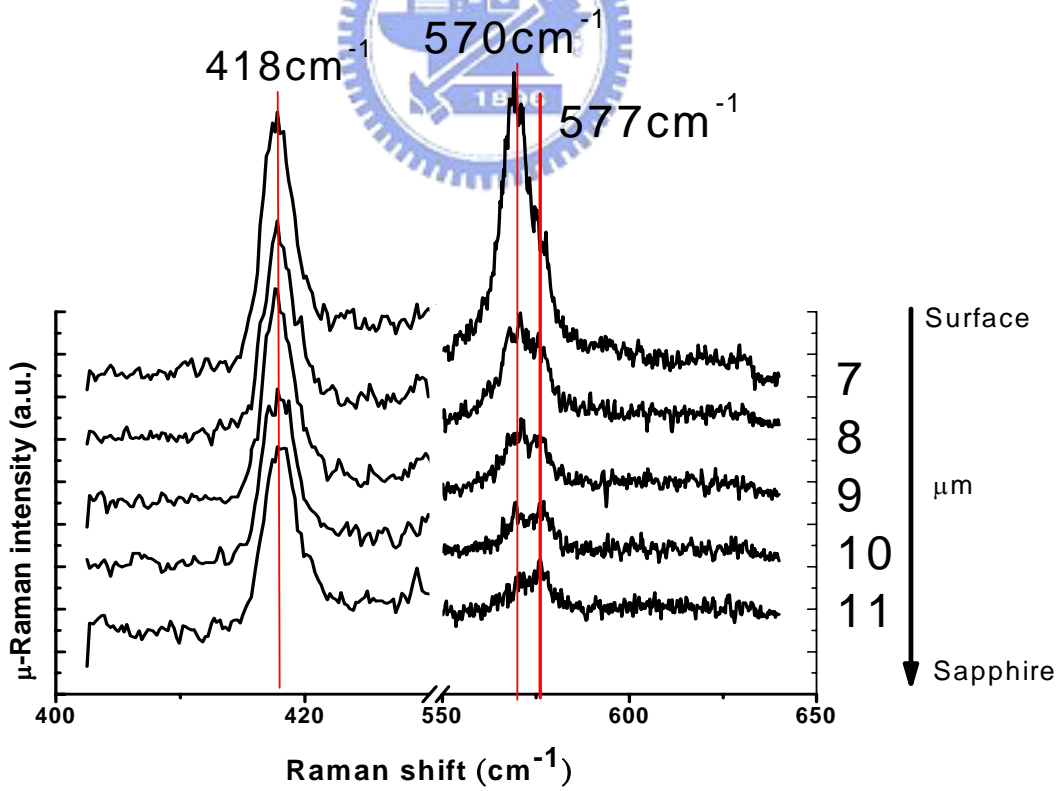
4-5-1 (b)

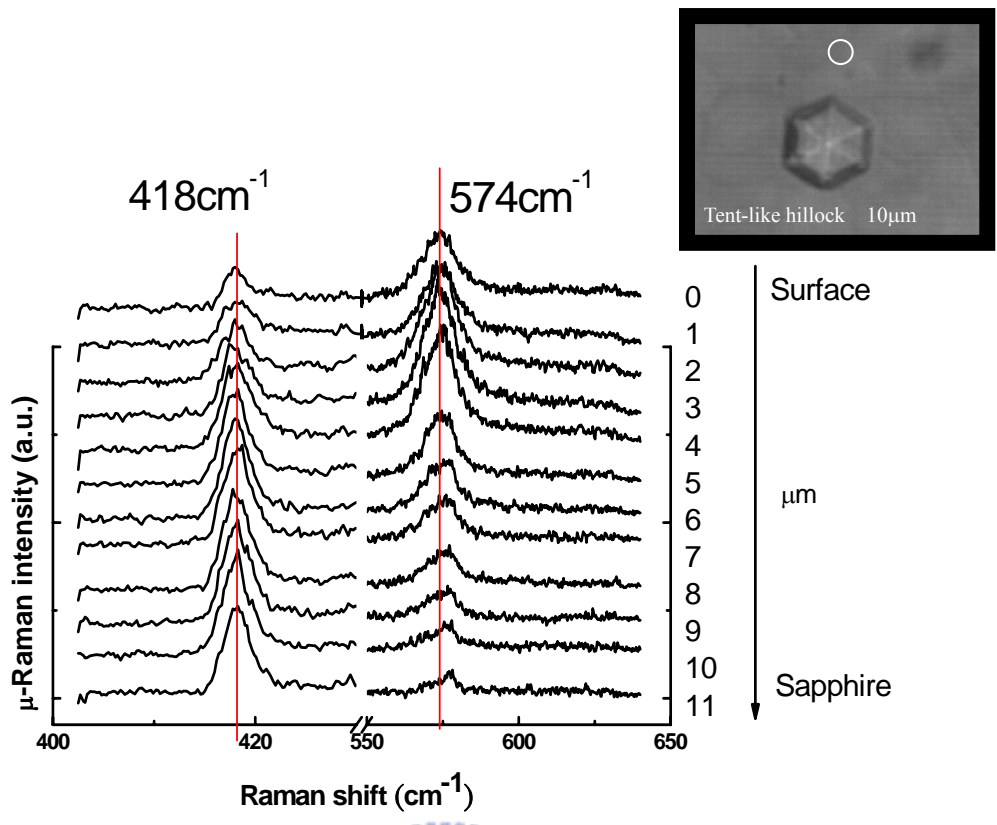**Hillocks grow from the AlN buffer**
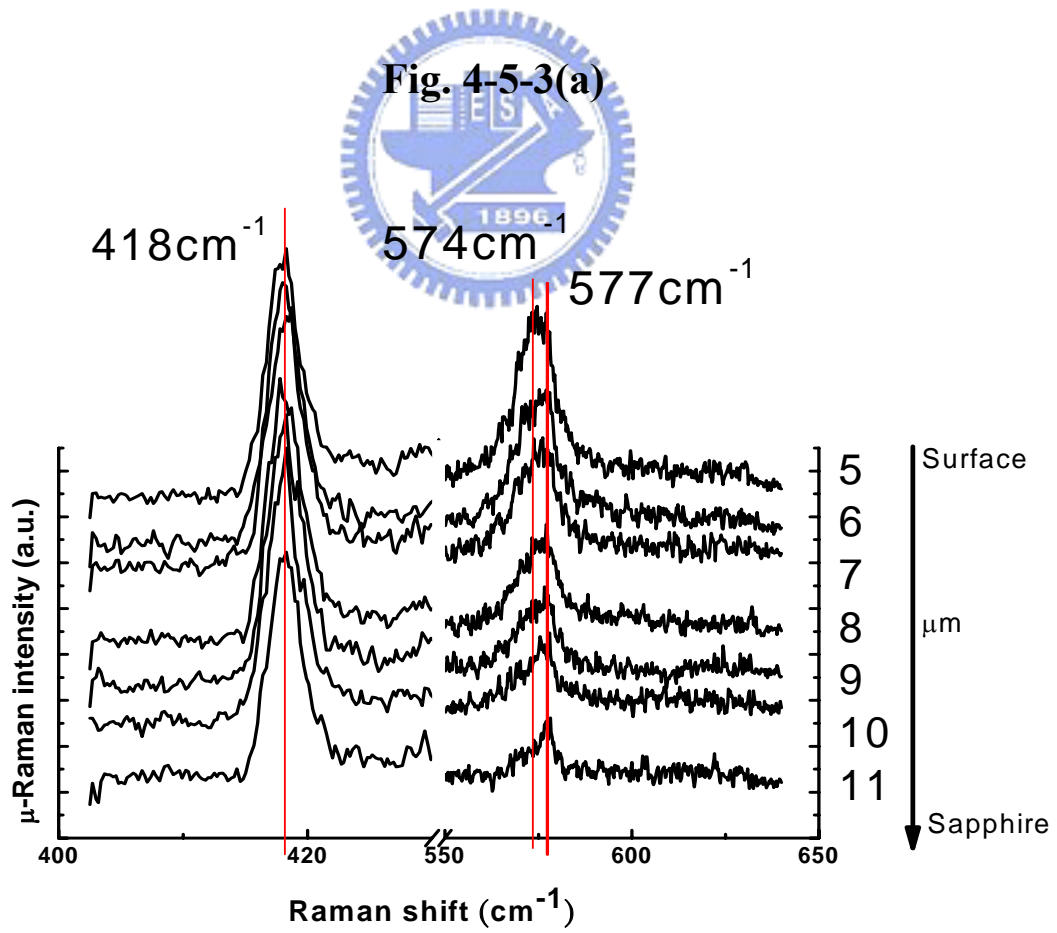
Fig. 4-5-2 (a)

Fig. 4-5-2(b)

Fig. 4-5-3(a)

Fig. 4-5-3(b)

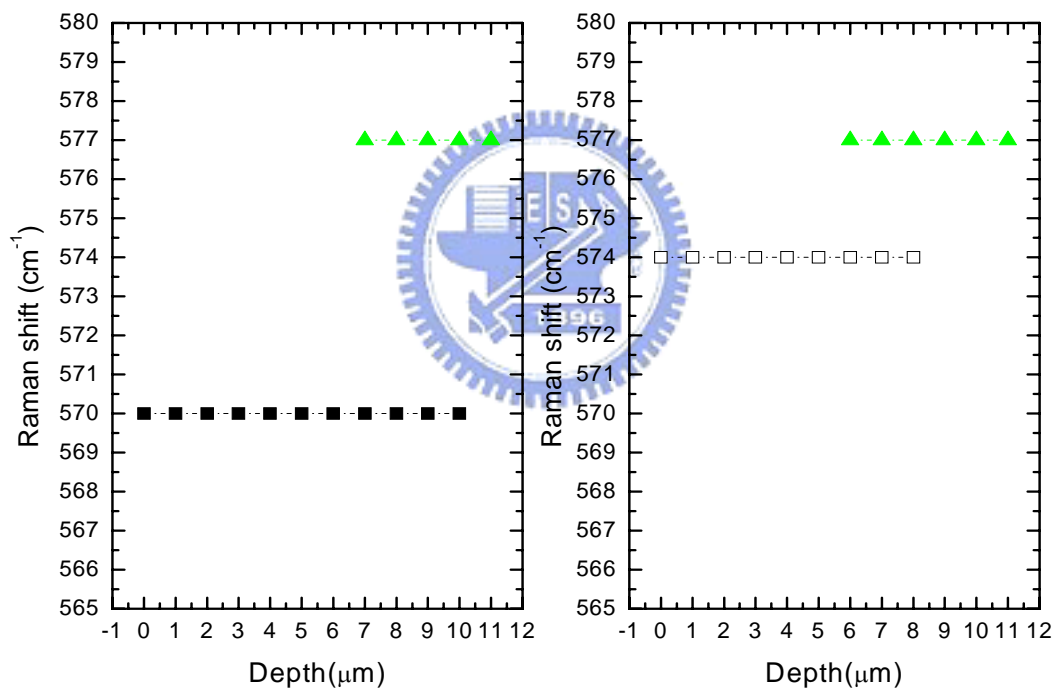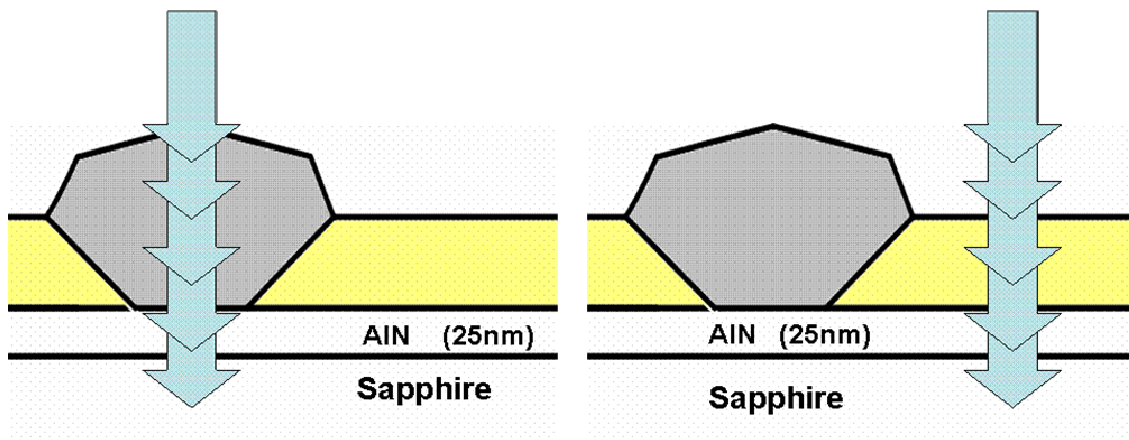**Fig. 4-5-4**

Chapter 5 Conclusion

In this thesis, we had studied spontaneously formed hexagonal hillocks on $Al_xGa_{1-x}N$ thin film. We utilized the spatially resolved μ-PL and μ-Raman techniques to characterize the optical properties across hillocks. By correlating the μ-PL and μ-Raman results, the influence of stress on hillocks is manifested.

The μ-PL results showed that an additional peak I_H appears at ~353nm in a (10μm) tent-like hillock besides the I_{NBE} emission at ~342nm. This phenomenon is attributed to the Al concentration and stress variations. From the EDX measurements, we know that the Al fraction is different from the inside to the outside of hillocks that agrees with the deduction from μ-PL. Moreover, the PL results are relatively insensitive to the strain, and the Al fraction deduced from μ-PL spectra is ~4% and ~11% inside and outside of the (10μm) tent-like hillock, respectively. For this Al fraction, we calculated the strain free E_2 mode frequency to be ~568.5 cm^{-1} and ~ 570.2 cm^{-1} inside and outside the hillock. By using the microscope to demarcate the hillock position, we used μ-Raman to study the same 10μm tent-like hillock. The experimental results showed that the E_2 mode frequency is ~570 cm^{-1} and 573 cm^{-1} inside and outside the hillock, respectively, so that they are deviated by ~1.5 cm^{-1} and ~3 cm^{-1} from the strain free E_2 mode frequency.

Moreover, we discussed the stress influence on optical properties of tent-like hillock of various sizes. From the μ-PL spectra, the peak position is red shifted by 3.1 nm from 6 to 11 μm tent-like hillocks. This indicates that the Al fraction decreases progressively while the hillock size increases and the

variation is about 2% among these tent-like hillocks. The μ-Raman scattering was also performed on this series of hillocks. Inside each hillock, the E_2 mode frequency is ~570 cm^{-1}, and outside the hillock is ~573 cm^{-1}. Combing the μ-PL and μ-Raman results, the tent-like hillocks of various sizes bear less compressive stress than the outside region.

We also used μ-Raman scattering to investigate how deep hillocks are formed. The results showed that the E_2 mode frequency remains at ~570 cm^{-1} inside hillock, and it dose not shift while the focus depth increases. However, the sapphire E_2 mode frequency at 577 cm^{-1} grows obviously with the increasing focus depth. According to the depth analysis, it is evident that the formation of hillock is from the AlN buffer layer.